Raikoke Volcanic Sulfate/SO_2 Anticyclonic Contained Circulations: in situ Proof, Morphology, and Radiative Signature

M. D. Fromm[1*], G. P. Kablick III[1], I. A. Taylor[2], R. G. Grainger[2], C. Seftor[3], E. J. Welton[4], J. Fochesatto[5]

[1]US Naval Research Laboratory, 4555 Overlook Ave., S.W., Washington, D.C., 20375, USA
[2]COMET, Sub-Department of Atmospheric, Oceanic and Planetary Physics, University of Oxford, Oxford, UK
[3]Science Systems & Applications, Inc., Lanham, Maryland, USA
[4]NASA Goddard Space Flight Center, Greenbelt, Maryland, USA
[5]University of Alaska, Fairbanks, USA

Key Points:

- Intense concentration of liquid sulfate aerosol is present in the stratospheric Raikoke volcanic cloud in its nascent phase.
- Lidar and in situ radiosonde-balloon data confirm anticyclonic circulation within Raikoke's distinctive compact SO_2/sulfate clouds.
- Infrared absorption within the sulfate/SO_2 compact clouds indicates localized warming leading to diabatically-driven self-lofting.

*US Naval Research Lab, Remote Sensing Division, 4555 Overlook Ave., SW, Washington DC 20375

Corresponding author: M. D. Fromm, michael.d.fromm4.civ@us.navy.mil

Abstract

We present an analysis of the stratospheric cloud from the June 2019 Raikoke volcanic eruption. The cloud is observationally characterized herein as consisting primarily of SO_2 and sulfuric acid droplets, and marked by multiple distinctive, quasi-circular cloud features ∼300-400 km in diameter. Previous reports showed that one of these entities was traceable for three months. Anticyclonic circulation was also previously reported. We present multiple lines of evidence to characterize these cloud sub-elements by their spatial confinement, morphology, and sulfate-dominated aerosol aspect, which was evident from plume onset. In addition, we show that they were ably identifiable in geostationary satellite "cirrus channel" reflectance imagery and had an enduring signal of window infrared absorption, detectable for at least one month. The term we apply to this phenomenon is "sulfate/SO_2 anticyclonic contained circulation," abbreviated SSACC. Anticyclonic circulation is first detectable on 24 June, 2 days post eruption. Two SSACCs persist beyond June. One is traceable until mid-August over Canada. The other SSACC was discernible until 5 October after having completed three global circumnavigations. The internal SSACC circulation aspect is gleaned from geostationary-based visible-image animations and confirmed in situ via a novel application of high-resolution radiosonde wind direction and balloon-position data. We also examine diabatic lofting of both SSACCs in relation to their individual geographic and constituent morphologies. Thermal infrared observations show that SSACC aerosols produce brightness temperature depressions of ∼2.6 K, opening a new line of investigation into the source of heating that contributes to diabatic rise.

Plain Language Summary

We present a satellite-based analysis of the stratospheric cloud from the 2019 Raikoke volcano eruption. The volcanic cloud consisted primarily of sulfur-containing gases and particulates marked by two previously reported near-circular cloud features. One of these clouds had been followed for three months and exhibited a surprising anticyclonic circulation. We present lines of evidence to characterize both compact clouds by their diameter, multi-month lifespan, and composition. These predominantly liquid sulfate clouds show up as early as three days post eruption. The satellite data presented herein indicate that comingling of SO_2 and sulfate particles is a characteristic nearly from inception. These clouds absorbed terrestrial infrared radiation. The term we apply to this phenomenon is "sulfate/SO_2 anticyclonic contained circulation," or "SSACC." Two SSACCS are followed from 24-25 June (2-3 days post eruption). The circulation aspect is confirmed by combining visible satellite images, ground-based lidar, and radiosonde wind and balloon-position data. We also examine self-lofting of both SSACCs; they rise considerably beyond Raikoke's injection height. The holistic view of all satellite-based observations shows that SSACC composition was active in the terrestrial part of the spectrum, signifying the likelihood of infrared radiation contributing to observed self-lofting.

1 Introduction

Raikoke volcano (48.292°N, 153.25°E), located in the Kuril Island chain (Crafford & Venzke, 2019), erupted explosively into the stratosphere on 21-22 June 2019. This stratospheric eruption plume has garnered intense scrutiny, owing to its considerable SO_2-mass source term (de Leeuw et al., 2021) and eventual sulfuric-acid-cloud spread and persistence (Boone et al., 2022). The evolution of the Raikoke volcanic cloud within the week post eruption has been established (Kloss et al., 2021; Osborne et al., 2022).

The Raikoke eruption generated peculiar plume elements that were the subject of, or recognized in, several reports. In short, they appear on maps as horizontally quasi-circular SO_2/aerosol features that stood out from the overall Raikoke cloud in terms of persistence and localized sulfurous concentration. Apparent diabatic rise in the strato-

sphere well beyond injection height was also a characteristic. Chouza et al. (2020) identified one such element in late September over Hawaii and traced it back to the northern Pacific Ocean in mid-July. Gorkavyi et al. (2021) (hereafter G21) also focused on this feature and named it a "coherent circular cloud." They also identified a second, fleeting occurrence south of Alaska in late June. The persistent cloud element was sufficiently dominant that it was revealed obliquely by Cameron et al. (2021) and referred to as Raikoke's "secondary plume" by Knepp et al. (2022). This peculiar Raikoke residual and a second persistent quasi-circular cloud element, both termed "compact SO_2 cloud" by Cai et al. (2022) (hereafter "C22"), were traced from 10 July to August.

Both C22 and G21 put a focus on the transport and shape maintenance of the compact Raikoke cloud element that drifted to subtropical latitudes before circling the globe. They used trajectory models in this attempt. C22 found that no trajectory model settings led to a successful maintenance of the compact cloud element's size or shape beyond ∼3 days of initial conditions. G21 offered two hypotheses for the persistence of the compact cloud structure: simple transport in a shear-free environment (called the "dead fish") and containment in a gyre (called the "great red spot"). Their analysis led to the "dead fish" determination.

The circulation aspect of the G21 and C22 compact cloud was directly addressed by Khaykin et al. (2022) (hereafter "K22"), who showed by means of satellite-based Doppler lidar that these entities embodied anticyclonic winds, thereby consistent with G21's "great red spot" construct.

K22, C22, and G21 all acknowledged the diabatic ascent of one of these compact cloud elements. According to K22, such a circulating and diabatically rising volcanic cloud had not been identified in any previous stratospheric volcanic event. K22 attributed the rise to internal heating by radiative absorption by residual ash. They also associated this phenomenon with another recently discovered stratospheric particulate spheroidal circulation composed of wildfire smoke (Allen et al., 2020; Kablick et al., 2020; Khaykin et al., 2020; Lestrelin et al., 2021; Allen et al., 2024). The smoke-clouds' diabatic rise was attributed to heating due to absorbing aerosol interaction with incoming solar radiation. The absorbing aerosol diagnostic, satellite-based ultraviolet aerosol index, was shown to be a clear marker that persisted for weeks (Allen et al., 2020, 2024; Khaykin et al., 2020). This naturally raises the question as to whether these apparently similar physical phenomena, generated by different sources and comprising wholly different constituents, are niche peculiarities or rather a scientifically important aspect of stratospheric-cloud composition, dynamics, and radiative impact. To address the questions, more observations and analysis are needed. Herein we introduce several lines of observational evidence to characterize the Raikoke compact volcanic cloud elements and offer new arguments for the agent of diabatic rise. The end result of the SO_2 to particle conversion process is sulphuric acid although in the troposphere further reactions can give rise to salts such as ammonium or sodium sulfate. Here and elsewhere, "sulfate" is adopted as all particle forms contain the SO_4^{2-} anion and we introduce the term Sulfate/SO_2 Anticyclonic Contained Circulation (SSACC).

Although diabatically rising discrete volcanic clouds have not been observed prior to Raikoke, diabatic stratospheric thermal and dynamical perturbations have been identified in the aftermath of the major volcanic eruptions of El Chichón in 1982 (Labitzke et al., 1983) and Mt. Pinatubo in 1991 (Labitzke & McCormick, 1992). The stratospheric warming in these two sulfuric acid clouds was attributed primarily to longwave terrestrial infrared radiation by the clouds' sulfuric acid aerosols. Such was the impact of the Pinatubo aerosols on thermal infrared (IR) absorption that satellite broadband IR-based sea-surface temperature retrievals were negatively biased for approximately one year post-eruption (Reynolds, 1993). Hence it is conceivable that dense concentration of Raikoke sulfates would have a similar IR absorption feature. This is one aspect of the compact Raikoke SSACCs we explore herein.

Our analysis is based on an ensemble satellite-data approach to follow the particulate and gaseous SO_2 evolution of the overall Raikoke cloud with a focus on the two circular compact cloud entities identified by C22 and K22. We also employ high-resolution radiosonde atmospheric and GPS-position data. A considerable emphasis is placed on geostationary-satellite visible and IR data in the form of animations, which are included Supporting Information.

2 Data

2.1 IASI

In this study, two SO_2 retrievals have been applied to data from the Infrared Atmospheric Sounding Interferometer (IASI), an instrument onboard the MetOp platforms (for information see Blumstein et al. (2004); Clerbaux et al. (2009)), and data from all three instruments have been used when available (note that the number of instruments available varies over the time period studied). An advantage of the IASI instrument is that each instrument obtains near-global coverage twice a day, so offering increased temporal coverage compared to UV instruments. This allows for better tracking of the SSACCs. A linear retrieval, described in Walker et al. (2011, 2012), was used to identify pixels which have elevated amounts of SO_2. This product was used to locate the SO_2 from the Raikoke eruption. Using maps of the linear retrieval results, boundaries of the two SSACCs were manually drawn and recorded.

An iterative SO_2 retrieval was applied to pixels flagged by the linear retrieval. This method iteratively fits the top-of-atmosphere spectrum by varying the state vector until a good match is found with the measured spectrum. The state vector includes the SO_2 column amount in Dobson Units (DU), the height in pressure (the result is later converted to kilometers), the cloud thickness (1σ thickness strongly constrained to 30 hPa) and the effective radiating temperature. The retrieval also produces comprehensive error estimates for each parameter. These errors are computed using an error covariance matrix which represents spectral variability between the measured and simulated spectra, thereby incorporating errors associated with the instrument noise, the presence of cloud, forward model errors, errors in the meteorological data and spectroscopy errors. Full details of the retrieval can be found in Carboni et al. (2012, 2016). Over time, as the amount of SO_2 decreases, there is less sensitivity to the height of SO_2 leading to the result tending to the *a priori*. This is especially the case in the dry stratosphere. Subsequently in this study, four heights *a priori* are used to represent different parts of the Raikoke SO_2 cloud: 1. Standard Configuration/Full plume (21 June-1 July); the retrieval was run using its standard height *a priori* (400±500 hPa) as in Carboni et al. (2012, 2016, 2019), and the values reported in Table 1 and Figure 1 and 3 are based on this version, 2. Full plume (1 July-28 August); the height *a priori* (183±300 hPa) is based on the median for pixels with heights in the stratosphere obtained with the standard retrieval setup for the period 21-24 June 2019, 3. North SSACC (1 July-28 August); a height *a priori* of 66.5 hPa is based on the average Cloud-Aerosol Lidar with Orthogonal Polarization (CALIOP) cloud top heights using an 0.01 extinction threshold for this SSACC, and is highly constrained to agree with the average CALIOP cloud top height, 4. South SSACC (1 July-28 August); the cloud top heights (0.01 extinction threshold) from CALIOP cloud show that the height of this SSACC increases over time. A linear fit has been applied to these heights and this has then been used to set the *a priori* height for each day with a very small uncertainty so that the height retrieval is constrained to agree with the CALIOP value.

These *a priori* values have also been used as the first guess. In each case, the SO_2 column amount *a priori* and first guess have been set to 0.5 ± 100 DU and the effective radiating temperature *a priori* and first guess have been set based on the European Centre for Medium-Range Weather Forecasts (ECMWF) data with an *a priori* uncertainty

of 20 K. A quality control, as described in Carboni et al. (2012, 2016), is applied to the results. An example of where the quality control may remove pixels is in cases where there are significant quantities of ash which would lead to a poor match between the modeled and measured spectra. For example, Carboni et al. (2012) shows that the SO_2 retrieval is affected when in the presence of ash with an optical depth of 1. An optical depth of 2 is then shown to cause a 50% underestimation of the column amount, while an optical depth of 5 would completely mask the SO_2 signal (Carboni et al., 2012). In the case of Raikoke, it is notable in the first week after eruption that the core of the cloud (Figure 1 and 3) is masked out due to the result not passing the quality control, which may be related to the presence of ash, elevated levels of sulfate or other factors which might lead to a poor correspondence between the simulated and measured spectra.

The data for each day have been divided into ascending (∼9:30 PM local time at the equator) and descending (∼9:30 AM local solar time at the equator) orbits. A discontinuity can occur where the date changes. To minimize the impact of this discontinuity, the descending results have been offset from the ascending by 12 hours. Subsequently, while the ascending results are a composite of ascending orbits from 00:00 to 23:59 on each day, the descending results are a composite of descending orbits from 12:00 of the day stated to 12:00 of the following day. Descending results are referred to by their start date. The data are gridded to a regular 0.125° by 0.125° grid, following which the column amounts and their errors are converted to a mass. Following the creation of a mass grid, the masses can be summed to compute a total mass for each time step. The total mass errors are also computed in this way.

2.2 OMPS

The Ozone Mapping and Profiler Suite (OMPS) Nadir Mapper (OMPS-NM) aboard the NOAA-20 (N20) satellite is the source for the ultra violet aerosol index (UVAI) data. The UVAI used here is the heritage product determined as a byproduct of the ozone retrieval algorithm and utilizes the 331-360 nm wavelength pair; for details of the algorithmic retrieval see Herman et al. (1997). Daily level 2 UVAI data have a resolution of 12.5 km across-track by 17 km along-track at satellite nadir; at the orbital image-swath edge the along-track resolution increases to 45 km, while the along-track remains at 17 km. The nominal local overpass time for the North Pacific International Dateline region we explore spans the range from 13:40 to 13:55. In this longitudinal zone, the measurement UTC is generally near 00 UTC. The local date of each daytime image analyzed herein may span two UTC days. Hence, imagery will be accompanied by the local date and the specific UTC range of the data therein.

2.3 CALIOP

We identified Raikoke cloud features of interest by manual association of CALIOP data with IASI SO_2 enhancements attributed to SSACCs or other notable cloud elements. The results are accounted for in Supporting Information Analysis S1. To characterize cloud height, aerosol optical depth (AOD), and particle type, we present data from the CALIOP instrument (Winker et al., 2009). The products used herein are Level 1b calibrated 532 nm total attenuated backscatter coefficient (β_{532}) and the perpendicular backscatter coefficient ($\beta_{532,\perp}$) used to derive the volume depolarization ratio (δ). Single-profile AOD is computed in accordance with CALIOP documentation by determining a per-profile lidar noise profile, calculating particle-only extinction from the total signal using a molecular threshold (Vaughan et al., 2005), and then vertically integrating all particle extinction coefficients within the identified vertical cloud boundaries. β_{532} is reported on a constant altitude grid, and cloud potential temperature (θ) is determined using MERRA-2 (Modern-Era Retrospective analysis for Research and Applications, Version 2) temperature and pressure data contained in the Level 1b data files. Two types of AOD calculations are used in later sections: a mean AOD (AOD_{mean}) and a maximum-possible

AOD (AOD_{max}). AOD_{mean} is the horizontal average of individual AOD profiles along the identified aerosol layers, and AOD_{max} is the vertical integration of a composite extinction profile, consisting of the maximum extinction value at each altitude along the aerosol layer. In other words, at each fixed-altitude CALIOP range bin across the scene, the maximum extinction is recorded and assembled into a single composite profile, and then integrated. This technique allows us to avoid the single-shot full attenuation CALIOP AOD limit ~ 0.3 that may bias the AOD low for extreme amounts. However, we note that the results derived from the AOD_{max} value should be considered qualitative as no validation of it has been made. Comparisons between AOD_{mean} and AOD_{max} profiles are shown for all CALIOP observations in Supporting Information Analysis S1.

We use the conventional definition of $\delta = \beta_{532,\perp}/(\beta_{532} - \beta_{532,\perp})$ in this study, which provides a quantitative indicator of aerosol sphericity. We derive a statistical analysis of δ from the Raikoke observations by relying on the particle-only signal mentioned above. Our procedure is the following: 1. subset the Level 1b data files by visual determination of Raikoke plume location, 2. calculate single-pixel δ, 3. select δ pixels that are within -2.0 to $+2.0$ (-200% to $+200\%$) to remove single pixel noise spikes from statistics, and 4. use a coincident particle-only β threshold of 1.0×10^{-4} (km sr)$^{-1}$. We report both the mean and median δ values for each plume observation.

2.4 MPLNET

The NASA Micro Pulse Lidar Network (MPLNET) (Welton et al., 2001) is a global, federated network of continuously operating lidars collocated with the NASA AERONET (Holben et al., 1998). MPLNET data are collected continuously at a 1 minute data rate, and 75 meter vertical resolution from the surface to 30 km above mean sea level. MPLNET calibrations and signal processing are described by Campbell et al. (2002); Welton & Campbell (2002); and Welton et al. (2018). The MPLNET Level 1 Normalized Relative Backscatter (NRB) signal product is detailed online (`https://mplnet.gsfc.nasa.gov/product_info`), and includes the range, lidar signal, and the volume depolarization ratio. MPLNET Level 1 signals from the Fairbanks site on 6-7 July 2019 are presented here.

2.5 GOES and radiosondes

Cloud-image snapshots and animations from geostationary visible and near-IR reflectance, and window IR brightness temperature are used to characterize SSACC presence and cloud circulation. National Oceanic and Atmospheric Administration (NOAA) Geostationary Operational Environmental Satellite (GOES) Advanced Baseline Imager (ABI) West and East instruments are used. We use level 2 data at native 10-minute resolution. Maps and animations are generated using NOAA's Weather and Climate Toolkit (`https://www.ncdc.noaa.gov/wct/`).

We exploit high vertical resolution radiosonde data (Love & Geller, 2013) consisting of temperature, pressure, wind direction, and global-position-system (GPS) location recorded at 1-s intervals. This leads to an effective vertical resolution of $\sim$5 m (Geller et al., 2017). Such high vertical resolution data have been effectively used to examine fine-scale turbulence structures in the troposphere and stratosphere (Ko et al., 2019). We avail ourselves of the wind-direction and GPS coordinates for radiosondes launched at Fairbanks, Alaska, USA on 7 July 2019.

3 Results

3.1 Ash evolution in the nascent Raikoke Plume

On 22 June (local time), the first full day after Raikoke-eruption onset, the volcanic cloud had a relatively confined footprint with combination of SO_2 and ash concentra-

tion (Kloss et al., 2021), which immediately afterward separated into ash-dominated and SO_2-dominant segments (Figure 1). The ash mass was reduced by 90% according to infrared image-based retrievals by ∼25 June (Prata et al., 2022). This evolution is consistent with the UVAI, which recorded a strong positive signal on 22 June, a much weaker signal on 23 June, and loss of signal after 24 June (Figure 1). The positive side of the UVAI (Torres et al., 2020) is strongly and positively correlated with absorbing aerosol optical depth and altitude, such that stratospheric clouds comprising absorbing aerosols (ash, dust, smoke) are traceable for days to weeks after onset (Allen et al., 2020; Fromm et al., 2010; Torres et al., 2020). Hence the diminishment of this positive UVAI signal within three days of the eruption is a qualitative indicator that stratospheric volcanic ash became a minor constituent in the SO_2-dominated portion of the stratospheric Raikoke cloud established by the above-mentioned reports. However, it must be recognized that trace amounts of ash are likely to have been blended within the SO_2-dominated Raikoke cloud in its early evolution. We elaborate on this in our presentation of additional data items to characterize the gaseous and particulate nature of the evolving Raikoke cloud.

3.2 Raikoke SO_2 overview

The entire Raikoke SO_2 cloud two weeks post eruption is shown in Figure 2, using the IASI linear retrieval output. The SO_2 concentration on 6 July illustrates both the general spread of detectable sulfur enhancements as well as all local maxima. (An animation of the full set of IASI ascending and descending observations is contained in Supporting Information.) By this date the Raikoke cloud had expanded to stretch continentally from East Asia, across North America to Europe, and from midlatitudes to the high Arctic. Multiple local SO_2 maxima, in the form of stretched filaments and compact cells, are embedded within this broad SO_2 entity. The cells are the focus of our study. In Sections 3.3 and 3.4 we introduce complementary particulate and gaseous satellite-imager-based map views of the Raikoke cloud in the critical post-eruption period.

3.3 Tracking nascent Raikoke SO_2 and sulfate aerosol

Figure 3 contains mapped OMPS scattering aerosol index and descending IASI SO_2-concentration images from the iterative retrieval for every second day, 23 June–3 July. (A full set of daily maps out to 6 July is provided in Supporting Information Figure S1). The UV scattering aerosol index is a critical, previously unreported aspect of the Raikoke cloud's synoptic and mesoscale sulfate-aerosol evolution. The datum is the negative counterpart of the UVAI. Torres et al. (2020) succinctly summarize the UVAI spectrum's interpretation: "UVAI yields positive values in the presence of absorbing particles, near-zero for clouds, and small negative values for non-absorbing aerosols." Hereafter, we will refer to positive UVAI as the "absorbing aerosol index" and negative UVAI as the "scattering aerosol index." Penning de Vries et al. (2009) presented a general, formal introduction to the scattering aerosol index. To first order, enhanced scattering aerosol index (i.e., departure from zero in absolute value) signals enhanced concentration of scattering aerosols such as volcanic sulfates. This datum has been shown to reliably identify the presence of nascent UTLS sulfate clouds from the eruptions of Nabro (Eritrea) in 2011 and Hekla (Iceland) in 2000 (Fromm et al., 2013; Penning de Vries et al., 2014; Rose et al., 2003). Only negative UVAI pixels are mapped in Figure 3. The displayed pixels exhibit a magnitude exceeding three standard deviations from zero, calculated from a set of scattering aerosol index measurements within this domain on 21 June, the day prior to the eruption. Hence, they all represent a notable enhancement. The maps are color scaled relative to the post Raikoke scattering aerosol index maximum, observed on 23 June. It was noted in Section 3.1 that on 22 June the entire Raikoke cloud at OMPS time embodied a positive (i.e. absorbing) UVAI, consistent with a single, compact cloud dominated by ash. By 23 June the ash had primarily separated geographically and diminished greatly (See Figure 2 of Kloss et al., 2021) when the scattering aerosol index

first became manifest within the SO_2-dominated cloud element. On each day thereafter, well into July, the scattering aerosol index signal remained robust. The cloud on 23 June consists of a single, coherent structure. It deforms on subsequent days into a field of distinct, concentrated local maxima and connected streamers of subtler enhancement. On a qualitative level, the scattering aerosol index evolution displayed in Figure 3 reveals a nascent UTLS sulfate presence, akin to volcanic clouds such as that generated by Mt. Pinatubo (Guo et al., 2004), coinciding with SO_2 cloud features.

It is obvious that essentially all SO_2 features coincide with scattering aerosol index enhancements, noting minor differences attributable to the ∼3 h measurement-time offset between the two platforms. Hence it is apparent that UTLS sulfate aerosols were co-present in the SO_2-bearing Raikoke cloud from 23 June onward. Corroborating this, we present Figure 4, mapped 9.6 μm sulfate AOD on 3 July, to compare with Figure 3 k,l. This product, from the Rutherford Appleton Laboratory Infrared/Microwave Sounder retrieval system (Legras et al., 2022, and references therein), is predominantly influenced by IASI data. The maximum sulfate AOD, marked by the red open diamond, is 0.13. In Figures 4 and 3 k,l we see that the two SSACCs and the connected streamers all exhibit quantifiable sulfate AOD matching the qualitative UV scattering aerosol index features, both of which align with IASI SO_2 enhancements. The high correlation between the SO_2 and scattering aerosol index signals implies that the gas retrievals are a reliable proxy for aerosol presence as we demonstrate in Section 3.6.1. Detectable SO_2 persists well beyond the scattering aerosol index lifetime while carrying the inference of Raikoke sulfates for the expanded period analyzed herein. In the following sections we will invoke GOES and CALIOP data for representing Raikoke aerosol in horizontal and vertical dimensions.

The qualitative sulfate signal represented by the UV scattering aerosol index does not rule out the presence of residual ash. It will be shown in Section 3.4 that additional data items such as CALIOP backscatter curtains both confirm the presence of abundant Raikoke aerosols from the earliest hours after eruption, but also contain signals suggestive of solid particles in the cloud segments coincident with OMPS scattering aerosol index enhancements through 1 July. For this reason, selected Figure 3 panels contain orbit markers of Cloud-Aerosol Lidar and Infrared Pathfinder Satellite Observations (CALIPSO) utilized in the analysis described next.

3.4 Quantifying nascent Raikoke stratospheric aerosol and SO_2

Quantifiable stratospheric aerosol observations in the days following the Raikoke eruption are presented. The earliest CALIOP intercept of the cloud was on a daytime 22 June overpass while the eruption was ongoing. The lidar sampled the downwind (i.e., leading) edge of the cloud, corroborated by the orbital footprint on the descending IASI SO_2 and OMPS absorbing UVAI mapped imagery (Figure 1). Owing to its small horizontal extent and the noisiness of the daytime conditions, characterization of the aerosol signal is difficult. It is reported here simply for the record. The CALIOP feature's top altitude (z) and θ are ∼12 km and 350 K, respectively. Muser et al. (2020) (hereafter "M20") reported on another measurement of the daytime 22 June volcanic cloud by the OMPS-Limb Profiler quite close to its geographic center, assigning 17 km to the cloud's top. These two satellite observations were essentially simultaneous.

CALIOP's second encounter with the Raikoke cloud occurred on a nighttime pass on 22 June (Osborne et al., 2022), when z was ∼16.6 km, and θ was 424 K. This is consistent with the maximum extent of estimated Raikoke injection height based on geostationary satellite imagery (Horváth et al., 2021). Hence, on the day of the eruption, these three encounters provide useful–albeit incomplete–brackets on the range of observed stratospheric Raikoke cloud heights.

We continue the analysis with a detailed rendering of daytime Raikoke stratospheric aerosol encounters corresponding to selected descending IASI SO_2 and OMPS scattering aerosol index imagery in Figures 3. Figure 5 contains CALIOP curtains of β_{532} and δ for 23, 25, 29 June, and 1 July. In addition, we calculate AOD, layer-top z and θ, as well as layer-mean z, θ, δ_{mean}, and δ_{median}. AOD is calculated as discussed in Section 2.3 (Fromm et al., 2014). These values apply to the position within the feature of interest embodying the peak AOD, unless stipulated otherwise. Table 1 contains these values, along with neighboring SO_2 column and scattering aerosol index quantities. Considering the time difference between the IASI, OMPS and CALIOP overpasses and the likelihood that CALIOP did not sample a unified local SO_2 and aerosol maximum, the local IASI SO_2 maxima and OMPS scattering aerosol index minima orthogonally closest to the CALIPSO orbit segment are marked in Figure 3 and reported in Table 1. We note here that δ values from CALIOP Level 1b data can be larger than expected because of the noisiness of the daytime observations. For comparison, the nearest (in time) nighttime CALIOP observations of the same plume sub-elements shows δ_{mean} values of 0.22 (23 June), 0.29 (25 June), 0.18 (29 June), and 0.11 (30 June). A larger discussion on these CALIOP δ statistics is provided in Section 4.5.

On 23 June (Figure 5a,b), CALIOP sampled the Raikoke cloud through the core of the OMPS scattering aerosol index and IASI SO_2 cloud (Figure 3a and b, respectively). The layer is approximately 1 km thick. On 25 June, CALIOP sampled near the core of one of several localized SO_2/scattering aerosol index bodies (Figure 5c,d, 3c,d). Two Raikoke features dominate, a higher, optically thicker layer toward the south, centered near 56°N, and a lower structure extending to ∼61°N. On 29 June (Figures 5e,f, 3g,h) CALIOP sampled a strong core of SO_2 and scattering aerosol index near 58°N. On 1 July (Figures 5g,h, 3i,j), CALIOP sampled near the core of one of two nearby SO_2/scattering aerosol index bodies, near 54°N, 146°E. A relatively small but equally high aerosol feature to the north, and a lower, optically thinner and broader layer also occupy this curtain over areas of weaker IASI SO_2 enhancement (Figure 3j).

The four CALIOP samples in Figure 5 within locally intense Raikoke SO_2/scattering aerosol index bodies provide several important insights into the young volcanic cloud. They illustrate a strong aerosol concentration, dating to the immediate post-eruption condition. The peak AOD of these layers (Table 1) suggests a large and continuous particulate co-presence with IASI SO_2 abundance. There is also a general correspondence between variations in IASI SO_2 concentration and along-track CALIOP AOD, with the caveat that the measurement times are not coincident. The AOD along the cloud transects also correlates positively with the qualitative OMPS scattering aerosol index signal, providing corroboration that each feature's scattering aerosol index pattern fairly displays a direct relation between scattering aerosol and SO_2 abundance. Table 1 and Figure 5 indicate, albeit imperfectly owing to this selective analysis, that the Raikoke cloud through 1 July was within the altitude range of injection heights (Horváth et al., 2021).

The combination of IASI SO_2, OMPS UVAI, and CALIOP backscatter data presented above reveals that on no occasion since eruption was there an absence of volcanic aerosol amidst the gaseous sulfur cloud. From ash dominance on the first two days to sulfate prevalence thereafter, every IASI SO_2 signal was associated with volcanic particles. This coincidence of aerosol and SO_2 abundance will be corroborated in following sections with the incorporation of passive visible-image satellite data.

3.4.1 6 July Compact SSACC

Since approximately 1 July, the general Raikoke cloud was marked by two discrete compact sub-elements, according to Figures 3, K22, and C22. These two entities are the focus of the following sections, but here we perform a 3-dimensional exploration of an

individual compact Raikoke SSACC situated in nearly ideal view conditions. On 6 July the tandem of compact clouds was northwest of and over Alaska. The focal feature was over open water in almost totally cloud-free conditions. Figure 6a is a Terra MODIS true-color image of this gray, circular "cloud." Appendages on the north and south sides lead west (over a cloudy scene) and east (over northern Alaska), respectively. Figure 6b shows level 2 MODIS 550 nm AOD. It must be noted that the operational Dark Target MODIS aerosol retrievals (Remer et al., 2020) failed for this MODIS granule because the algorithm flagged a large core portion as cloud. An ad hoc AOD retrieval was forced on this granule by turning off the flags that were set. Hence, the absolute values of the AOD do not represent valid Terra MODIS retrievals. However, considering the homogeneously clear background, the geographic AOD pattern is considered to represent the visible cloud. As such, we see the expected radial increase of AOD from perimeter to core. IASI SO_2 and OMPS scattering aerosol index imagery for this scene are in Figure 6c and d, respectively. Measurement times of these various platforms are not identical (see the figure caption) but are small enough to allow comparisons. The UV, visible, and IR observations together confirm the volcanic nature of the circular cloud.

Vertical information about the SSACC is illustrated by the stratospheric CALIOP 532 nm β_{532} curtain in Figure 7a. The CALIOP transect nearly represents the entire circular SSACC (See Figure 6d), revealing the height, thickness and smooth topography of the aerosol layer. The CALIOP curtain extending to the Earth surface confirms the total absence of tropospheric cloud along the transect. CALIOP 532 nm AOD peaks at $\sim$0.35 in the along-track direction (Figure 7b). The AOD calculation is limited primarily by the assumption of lidar ratio, given the simplicity of the atmospheric aerosol/cloud profile within the SSACC along CALIPSO's path. We give bounds on this by calculating AOD with an assumed lidar ratio $\pm$10 from the chosen 60 sr. The resultant mean AOD is 0.21$\pm$0.04 for this SSACC on 6 July.

Our experimental Terra MODIS 550 nm AOD peaks $\sim$0.7. The MODIS and CALIOP AOD (Figures 6b and 7b, respectively) are in reasonable agreement with respect to cross-cloud variation. Hence the nadir-image AOD map can be considered representative of the SSACC's overall particle concentration, considering its co-registration with the IASI SO_2 and OMPS scattering aerosol index cloud. The OMPS scattering aerosol index appears to be a valid, albeit qualitative, proxy for particle concentration. Sulfate dominance as opposed to ash is also evident in that ash dominance at this altitude would elicit an unmistakably strong positive UVAI (Torres et al., 2020). CALIOP depolarization ratio is shown in Figure 7c with $\delta_{mean} = 0.16$ and $\delta_{median} = 0.11$. Figure S2 in Supporting Information shows a closer look at the depolarization ratio from Figures 5 and 7, and includes histograms of the pixels used in the statistics.

The 6 July case and the earlier snapshots of the Raikoke SSACCs reveal a general physical association among UV scattering index, visible AOD (MODIS, GOES, CALIOP) and IASI SO_2 concentration. It can be argued that the gaseous SO_2 signals of the young Raikoke cloud, both in general and specific to the SSACCs, are related to volcanic aerosol presence from inception.

Having established these combined volcanic gaseous and particulate markers, we now exploit them–and additional observations–in pursuit of our primary exploration of Raikoke's SSACCs.

3.5 IASI SSACC traceability

To unify and clarify SSACC terminology hereafter, we use "North SSACC" for the feature C22 called the "North America SO_2 cloud" and K22 called the "vorticized volcanic plume (VVP) II." "South SSACC" is the term for C22's "Asian Continent SO_2 cloud" and K22's "VVP I." The lower panel of Supporting Information Movie S1 shows the 'effective' SO_2 column amounts from the IASI linear retrieval for 1 July - 12 September

2019. This is termed 'effective' to reflect a number of assumptions made by the retrieval. Note that the colorbar range varies throughout the studied period. The first panel of the animation shows the paths that the two SSACCs travel as identified from the linear retrieval data.

In early July the two SSACCs are observed traveling across Eastern Russia and the Northern Pacific towards Alaska. Around the 7 July, the two SSACCs begin to take different paths. The North SSACC is initially transported southwards off the west coast of Canada and the United States, then around the 21 July this SSACC is transported northwards towards Canada. The North SSACC's journey is tracked across Canada up until 15 August. It may be possible to follow the SSACC for longer than this, but it became difficult to confidently define the boundaries of the SSACC past this date. In contrast, around 7 July, the South SSACC is transported back towards Kamchatka, following which it then moves southward and advects around the globe at $\sim 30^\circ$ N. This SSACC is shown to twice be transported around the globe between 20 and 30° N. The last confident detection of the SSACC in the IASI data is on 12 September 2019 (see Supporting Information Figure S3) but again it may be visible in the data beyond but the boundaries could not be confidently drawn.

The iterative SO_2 retrieval has been applied to quantify the column amount of SO_2 in each pixel. From this product the total mass of SO_2 for the full cloud and in each SSACC is determined for each time step between 1 July and the 15 August 2019 for the North SSACC and the 28 August 2019 for the South SSACC (Figure 8). This total mass is computed by summing gridded mass values for the region 20 to 90° N and -180 to 180° E. This means that any clouds from other eruptions occurring during this period and in this geographic range will contribute to the total masses reported. An exception is made in the first few days of the analysis (1-7 July) where the total mass is calculated for 30-90° N to reduce the effect of a large plume from Ulawun volcano in Papua New Guinea (Kloss et al., 2021). We cut off the time series at 28 August, as an eruption at Sheveluch in Kamchatka, produces a plume which would effect the total masses reported. A few outliers were removed from the time series. Some examples of where this was done include (1) dates where the SSACCs crossed 180 °E as this led to incomplete boundaries, (2) a few cases where the retrieval failed for the South SSACC and (3) a few cases where there was an error due to date changes in the South SSACC results.

The total mass of SO_2 across the full cloud (incorporating both of the SSACCs) is shown in Figure 8a, b. The starting total SO_2 mass is 0.68 ± 0.1 Tg which is shown to fall steadily over the two months studied, with an e-folding time of 12.8 days, which puts it in line with e-folding estimates for other high latitude stratospheric eruptions of similar magnitudes (Carn et al., 2016).

The total masses of the two SSACCs are shown in Figure 8c, d. The errors reported here incorporate those associated with the retrieval output but do not reflect the uncertainty resulting from the hand drawn SSACC boundaries. This subjective method might be the cause of some of the fluctuations which can be seen in the time series. Initially the total mass of the South SSACC (0.06 ± 0.001 Tg on 1 July Ascending orbits) is lower than that of the North SSACC (0.09 ± 0.001 Tg). The total mass of the North SSACC drops off more rapidly, with an e-folding time of 7.8 days compared to 9.0 days for the South SSACC. When the total mass of SO_2 with area is considered (Figure 8e, f), the highest concentrations of SO_2 is shown to be in the two SSACCs, which matches the maps shown in Supporting Information Movie S1.

3.6 Anticyclonic Sulfate Circulations

Next, we present several lines of observational evidence revealing that these Sulfate/SO_2 enclosures not only persisted in Raikoke's overall cloud for months, they exhibited anticyclonic circulation within two days of the eruption, and also manifested window in-

frared (IR) absorption, indicative of a causal mechanism for the observed heating and diabatic lofting reported previously and reinforced herein.

3.6.1 GOES Viewpoint, Early Post-eruption

It was established in Section 3.2 and 3.3 that soon after the eruption the Raikoke plume generated discrete, compact elements embodying coincident gaseous SO_2 and particulates. CALIOP data provided independent confirmation of aerosol presence conforming to these cloud elements. GOES visible-reflectance imagery is now used to further characterize these Sulfate/SO_2 entities. Illumination of the features is optimized from GOES-17's standpoint by taking advantage of enhanced forward scattering that occurs late in the day (low solar zenith angle) where satellite view angles are off nadir (for GOES-17, 137.2°W) toward the Sun. The SSACC target is ideally situated when it is west of satellite nadir and illuminated by the setting sun.

Figure 9 contains one such view over the Pacific Ocean generally north of the Aleutian Island chain on 25 June, 08:30 UTC. This late-afternoon shot is approximately 7-9 h after the OMPS scattering aerosol index and IASI SO_2 images in Figures 3d. In addition to the two primary SSACCs (marked with "+" for clarity), Figure 9 reveals additional volcanic cloud features corresponding to other local Sulfate/SO_2 maxima and streamers. Animation of the GOES imagery in Supporting Information (Movie S2, S3) allows a discernment of these various features as they evolve after the IASI/OMPS views. We note that this and other GOES visible animations are provided in pairs; 0.64 μm "red" channel and 1.37 μm "cirrus" channel. The cirrus band's advantage is that it effectively masks low clouds (Gao & Kaufman, 1995) that often dominate the scene. Notably, Gao & Kaufman (1995) also presciently recognized the cirrus channel's niche value for stratospheric aerosol detection. The red channel's advantage is a horizontal resolution four times that of the cirrus channel (0.5 km compared to 2 km for the cirrus channel) (Schmit et al., 2017). Within the animation, briefly before sunset, is the suggestion of anticyclonic motion around the SSACC centroids.

A second example of GOES visible imagery is provided in Figure 10 for the situation on 3 July. According to the OMPS scattering aerosol index and IASI SO_2 images in Figure 3, the Raikoke plume over the North Pacific has transformed into broadly distributed, relatively weak signals punctuated by two compact maxima east of Kamchatka, each with trailing filaments. Like the GOES images on 25 June (Figure 9), the 3 July GOES visible images are 7-9 h later with respect to IASI/OMPS. Even so, the stark visible rendering of the two compact features' geometry and surface-top texture confirms the co-presence of volcanic aerosol and gas. Note also the visual manifestation of particulate tails connected to each compact feature, also evident in the OMPS scattering aerosol index and SO_2 images (Figure 3). The animation sequence of GOES images leading to sunset 3 July (Supporting Information Movie S4, S5) provides strong qualitative indication that each SSACC is rotating anticyclonically. It bears noting that the synoptic-scale movement of these sulfate/SO_2 cores is entirely cyclonic from eruption to 3 July (Figure 3). Hence, if entity-scale anticyclonic circulation can be proved, it becomes evident that the rotation within these discrete cloud elements was generated and sustained within a steering environment of opposite circulation.

GOES visible imagery as presented above was examined twice daily, from 24 June to 13 July, except for times when the compact cloud elements were beyond GOES-17's limb or otherwise obscured. Centroid latitude/longitude locations were tabulated (Supporting Information) and displayed in Figure 11. This can be viewed in the context of Figure 16 of C22, who tracked and named two compact SO_2 clouds starting on 8 July. We see that the movement of the red color-coded South SSACC in Figure 11, the one situated to the south at initiation date, maps to C22's Asian Continent cloud whereas the blue path North SSACC matches their North America cloud. Figure 11 effectively

extends the long lifetime of these compact clouds back to the Raikoke cloud's nascent stage, when K22 first discerned them. It is seen that each feature transited cyclonically in the steering flow from onset to ∼3 July. They then both moved in tandem north to Arctic latitudes and were steered anticyclonically over Alaska before taking divergent paths forward. As intimated above, and demonstrated next, both Sulfate/SO_2 cloud elements manifested an enduring internal anticyclonic rotation, hence the SSACC terminology.

3.6.2 In Situ Confirmation of Circulation

The GOES visible imagery presented above (and additional examples provided in Supporting Information) elicited hints of contained circulation, albeit brief and subjective. Next, we combine GOES imagery with two additional probes of one of the compact Raikoke SSACCs to secure the determination of anticyclonic motions.

According to Figure 11 herein and Figure 16 of C22, both SSACCs moved over Alaska between 6 and 9 July. Fortuitously, C22's North America cloud blew over the NASA MPLNET (Welton et al., 2001) and radiosonde site at Fairbanks, Alaska (PAFA) between 6 and 7 July at a time when simultaneous, coincident profile measurements were made.

Figure 12 contains a GOES cirrus-channel visible image at 00:00 UTC 7 July. Fairbanks MPLNET and radiosonde-launch site are marked. At this time, one of the compact clouds is generally situated east of Fairbanks, its western fringe overhead of the site. At this time, the second compact cloud is out of view northwest of Alaska (Figure 6). Animation of this scene, from 20:00 UTC 6 July to 07:00 UTC 7 July is presented in Supporting Information (Movie S6). The animation once again provides visible suggestiveness of anticyclonic rotation, especially in this particularly low-sun-angle condition.

The MPLNET height-time curtain from 12:00 UTC 6 to 7 July is displayed in Figure 13. The SSACC moves into the lidar beam at ∼18:00 UTC and departs ∼13 h later; it is intermittently obscured by lower clouds (vertically-oriented gaps in lidar signal throughout the displayed altitude range). The Raikoke aerosol layer is roughly 900 m thick, from 15.9-16.8 km (θ=414-428K) at 00:00 UTC 7 July. Peak backscatter is at approximately 16.4 km, and the mean depolarization ratio within the Raikoke feature is 11.6%±9%. The cold-point tropopause, according to the Fairbanks radiosonde is at 12.4 km, 3 km below the layer center. It is noteworthy that the lidar was sampling a relatively weak portion of the SSACC; GOES imagery (Figure 12) suggests that the cloud-core backscatter (i.e., AOD) would be significantly larger.

The Fairbanks radiosonde launch, nominally at 00:00 UTC 7 July, was when the MPLNET signal of the Raikoke compact cloud was near its maximum. The balloon ascended through the western fringe (Figure 12). The next radiosonde launch at 12:00 UTC 7 July occurred after the cloud vacated the lidar beam. These two radiosonde measurements are shown in Figure 14. Wind-direction profiles for the SSACC and post-SSACC samples in Figure 14a are focused on 14-18 km to resolve important details. Included in Figure 14a is the lidar NRB profile at 00:00 UTC 7 July, revealing the altitude range and central peak of the Raikoke aerosols. Figure 14b is a map of radiosonde-balloon GPS position for the 00 and 12 UTC flights. For reference, the 00 UTC balloon position at its curvature is approximately 44 km from the Fairbanks MPLNET.

Wind direction was similar at 00 and 12 UTC 7 July below (northwesterly) and above (north to northeasterly), indicative of an unchanging synoptic-scale flow regime. However, at the time of the SSACC encounter, the wind direction diverged from that state at ∼16.2 km as the balloon ascended through the bottom half of the aerosol layer. Balloon movement was such that instantaneous wind direction cycled clockwise back to northwesterly near the layer top, ∼16.8 km. Above the sulfate layer the wind direction once again fell within the bounds of the post-SSACC conditions. The mapped GPS po-

sitions in Figure 14b illustrate that the 00 UTC balloon's horizontal trajectory was clearly altered as it ascended through the SSACC in the span of four minutes. The excursion would be consistent with expectations for an encounter with localized anticyclonic flow within a body positioned to the north and east of the balloon. The balloon's initial southeastward trajectory, driven by the large-scale steering flow, was evidently altered by a localized wind change within this layer. Considering its position with respect to the SSACC centroid (Figure 12), without this wind anomaly the balloon would not have deviated so drastically from its course being maintained by the steering flow. The apparent discontinuity in the wind direction in Figure 14 makes this clear. It must be noted here that the extremely fine, 1-s vertical radiosonde reporting translates to a resolution on the order of 5 m. The fortuitous coincidence of the GOES visible animation, lidar remote sensing, and in situ high-resolution radiosonde sampling offers a unique and unequivocal confirmation of anticyclonic circulation within both horizontal and vertical bounds of the SSACC.

A second example of a radiosonde SSACC encounter is given in Figure 15. On 10 July at 00:00 UTC South SSACC was positioned over southwestern Alaska, transiting roughly westward (Figure 11). At that time, the radiosonde launched from Bethel (Station ID "PABE") ascended through the western half of South SSACC. GOES visible-image animation (not shown) reveals that South SSACC was totally upwind of PABE 12 hours earlier and downwind 12 hours later. Figure 15a illustrates the SSACC-encounter wind-direction profile (00:00 10 July) as well as the two immediately preceding and following the encounter. Unlike the 7 July example, there are no contemporaneous lidar observations of the SSACC. In that absence, we estimate SSACC height range based on observations closest in time (See Supporting Information). Figure 15a shows that below and above the expected SSACC range the three wind profiles are largely overlapping and mainly easterly. Within the estimated SSACC range, the 00:00 UTC wind profile diverges considerably toward a southeasterly component. Figure 15b gives a map view of the 00:00 UTC situation. The inset reveals the radiosonde site and balloon position with respect to South SSACC. The zoomed-in view shows the details of the balloon's path below, inside, and above the SSACC. It is evident that the balloon's westward trajectory is perturbed to the north inside the SSACC. As with the 7 July SSACC encounter illustrated in Figure 14, this example reveals the effects of a localized anticyclonic forcing, hence a second instance of in situ proof thereof.

3.6.3 GOES Viewpoint: Month-old South SSACC

GOES-image support for the South SSACC extends at least through August 2019. Two examples are given, the first on 21 July. G21, C22, and K22 all focus on or about this date, over the North Pacific east southeast of the volcano near longitude 168°E. These reports and our Figure 11 show that the SSACC traces back to the nascent time frame and is about to embark on its journey to and fate within subtropical latitudes. K22 show Doppler lidar evidence of circulation on 21 July. Whereas these prior publications documented the horizontal image of the SSACC in terms of satellite SO_2 concentration, we emphasize the aerosol component in Figure 16. GOES "red" channel visible imagery of the SSACC at 03:00 UTC 21 July (Figure 16a) manifests a scene over the Pacific Ocean dominated by stratocumulus cloud and isolated patches of open water. The two interior circular marks are situated within the SSACC; the four outer ones are beyond the SSACC's visible perimeter, as brought out by the cirrus-channel visible image in Figure 16b. This preferential wavelength obscures the dominant cloud deck due to its low height. This is corroborated in Figure 16c, the accompanying "clean" window BT image, within which there is no hint of high/cold cloud in the vicinity of the SSACC. Animations are contained in Supporting Information (Movie S7). The IR BT depression within the SSACC will be discussed in Section 3.7. Like the previous examples from the early post-eruption days, the cirrus-channel image reveals a quasi-circular, contained cloud while both animations suggest an anticyclonic circulation. Given the establishment of the SSACC phe-

nomenon by way of the Fairbanks MPL and radiosonde data in early July, it is reasonable to infer continuous SSACC behavior. Additional support for the SSACC behavior of this compact cloud will be introduced in Section 3.8.

The second example invokes GOES-16 (GOES East) imagery 48 days post eruption on 9 August, when South SSACC was over the subtropical Atlantic Ocean west of Morocco (C22; K22). Figure 17 contains a still image at 07:10 UTC of the South SSACC soon after sunrise (optimal lighting for GOES East). The SSACC appears not only as the now familiar compact, quasi-circular structure, but also includes a demonstrable "tail" of trailing sulfate back over Mediterranean Africa. The tail, evident in many SSACC representations in G21, C22, K22, and herein, is likely to be associated with sulfate material shed from each SSACC. Once again, the animation (Supporting Information Movie S8) gives the hint of slow anticyclonic motion within the SSACC accompanied by general westward advection of it and the appended filament.

3.7 SSACC Thermal IR absorption

At certain intervals in the evolution of the two SSACCs, broadband IR imagery manifests perturbed window-IR brightness temperature within them. Here we highlight one such example, the South SSACC shown in Figure 16a and discussed in Section 3.6.3. Between 20 and 21 July, the visible SSACC was drifting slowly over the Pacific Ocean southeast of the Kuril Islands. Cloud conditions in the vicinity of South SSACC during the 36-h interval 12:00 UTC 20 July to 23:50 UTC 21 July were such that it was predominantly over a background of stratocumulus cloud or open water. This interpretation is bolstered by the window-channel 10.3 μm BT image from GOES West in Figure 16c at the same time as Figure 16a,b. We use a color bar and BT range that accentuates a BT anomaly in geographical concert with South SSACC. Figure 16c reveals a localized BT depression within the visible SSACC relative to the surrounding space. South SSACC minimum BT (269.37 K) is, on average, 3.46 K less than that of the three extra-SSACC, stratocumulus-covered pixels in Figure 16a. (The pixel south of the SSACC over mostly open water is 2.07K warmer than the average stratocumulus BT.) The persistence of this BT depression is illustrated in an animation of the above-mentioned 36-h period, provided in Supporting Information Movie S7. The animation manifests a subtle yet recognizable signal of anticyclonic rotation. Even with the degraded horizontal resolution of the GOES IR channel vis a vis the "red" visible channel (nominally 2.0 km vs. 0.5 km), the window IR data have the advantage of continuous feature viewing.

The window IR analysis affords a new insight, longwave absorption within the SSACC. The absorption is apparent during this favorable interval, but it was also evident at earlier moments within both SSACCs' lifetimes. An example during the period of 2-3 July (See also Figures 3k,l and 9) is contained in Supporting Information Movie S9. At that time both SSACCs were in close proximity and both exhibited IR absorption consistent with the 20-21 July encounter. Thus, the IR-absorption property of the SSACC appears to have endured throughout the month post-eruption. The most relevant implication may be that the SSACC embodies longwave absorption traceable to favorable particle size distribution and concentration. An enduring and substantial imprint of stratospheric volcanic sulfates on terrestrial IR absorption has been noted in the cases of the El Chichón (1982) and Mt. Pinatubo (1991) sulfate clouds (Reynolds, 1993; Walton, 1985) such that satellite-imager-based operational sea-surface temperature retrievals were negatively biased under the volcanic sulfate shroud. The longwave absorption of terrestrial radiation by the SSACC may then be a driver of the observed diabatic rise of the SSACCs reported by K22 and G21, and further explored next.

3.8 Diabatic Rise of the Raikoke SSACCs

The temporal height increase of the Raikoke SSACCs is assessed by combining IASI SO_2 concentration retrievals with intersecting CALIOP SSACC observations.

3.8.1 CALIOP SSACC-height evolution

As mentioned above, CALIOP orbits intersecting closest-neighbor ascending and descending IASI SSACC features were used to characterize the coincident aerosol-layer altitude, and AOD. When South SSACC was no longer detectable in the IASI SO_2 data, we manually followed its progress daily by identifying the most downwind orbit containing aerosol enhancement in its applicable altitude range (The cloud had sheared by this time such that it was evident in multiple contiguous CALIOP orbit segments). The results are plotted in Figure 18. Figure 18a illustrates SSACC AOD. Aerosol layer height/θ are plotted in Figure 18b, c, respectively. Granular detail of the set of CALIOP cloud and SSACC samples summarized in Figure 18 are contained in Supporting Information, Figure S4.

Several evolutionary aspects of both SSACCs are illuminating. During the period of North and South SSACC coexistence, their AOD is qualitatively equivalent (Figure 18a), generally consistent with the evolution of SSACC SO_2 mass density (Figure 8e, f). Also, the AOD typically exceeds the AOD of other CALIOP intercepts of the Raikoke aerosol cloud in the earliest days (see the black symbols in Figure 18a). I.e. SSACC particle concentration is large relative to extra-SSACC Raikoke cloud elements. Hence, both the aerosol and SO_2 quotient of the SSACCs stand out from the overall Raikoke cloud throughout their lifetime.

Both SSACCs rise above the injection-height peak ($\sim$16.8 km) on or about 13 July. After that point, all altitude increases can be unequivocally attributed to diabatic forcing. North SSACC increases in altitude quasi-continuously over the north Pacific and high-latitude North American continent, reaching a peak of 20 km ($\sim$482 K) on 21 July. Subsequently, North SSACC's altitude flattens between 18-19 km (455-475K). Prior to 21 July, during North SSACC's ascent, it was over Pacific oceanic background. Thereafter it was exclusively detected above the North American continent (See Movie S1). South SSACC's inexorable rise begins around 6-7 July when it is at Arctic latitude northwest of Alaska (See Figure 6). It rises without interruption until mid-September, when it levels off at 26 km (640K), as also revealed by K22.

South SSACC's rise-rate is calculated for selected sub-periods as illustrated in Figure 18b. The period of most rapid ascent (360m/d) ensues on $\sim$23 July when the SSACC is over midlatitude Pacific Ocean background (See Figure 16 and the IASI animation in Supporting Information, Movie S1.) This particular rise-rate calculation period extends to 4 August when the SSACC is over the Middle East (K22). However, the SSACC is over the western Pacific through 29 July. Hence this interval comprises roughly equal SSACC presence upwind of and over the Asian Monsoon zone (K22). It is thus difficult to attribute the locally extreme diabatic rise to any single background condition. Given the evidence of thermal IR absorption within the SSACC (Figure 16), we posit that this factor, evident on other days prior to the SSACCs passage over the Asian Monsoon zone, is the most likely and enduring forcing of SSACC heating and diabatic rise. North SSACC's diabatic rise terminated while its AOD and altitude were on par with South SSACC's (Figure 18). South SSACC's altitude continued to increase as it advected south and then westward, circling the Earth. Its leveling off appears to be associated with a diminution of AOD in its waning phase. Precise determination of the forces factoring into the diabatic lofting and eventual termination thereof is beyond the scope of this work but an important topic for further exploration.

4 Discussion

4.1 Evidence for Persistent Ash Dominance

M20 argue that ash-induced lofting generated in their model simulation is consistent with observations. For that they examined OMPS-LP profiles at 02:27 UTC 22 June in the vicinity of the umbrella cloud (illustrated in their Figure 3b) during the active eruption. Kloss et al. (2021) show this OMPS profile in their Figure A1. The preponderance of the Raikoke cloud layer is between the extinction maximum at 13.5 km and the topmost extinction enhancement at 16.5 km. Horváth et al. (2021) detailed the eruption-height chronology and found pulses as high as 16.5 km. Hence the OMPS cloud observation reported by M20 and Kloss et al. (2021) is within the range reported by Horváth et al. (2021). According to the latter study's eruption-pulse chronology, derived from 10-minute geostationary image data, the first injection clearly breaching the tropopause occurred at 01:20 UTC 22 June. Hence, this serendipitous OMPS sampling followed within 1-2 hours of the first stratospheric impulse. It seems less plausible for there to have been a rapid 3 km vertical transport of the Raikoke cloud (M20) than a direct injection to the heights revealed by OMPS-LP.

In addition to the above-mentioned OMPS-LP stratospheric aerosol layer, CALIOP detected a Raikoke feature well above the tropopause during a night-time encounter at 16:00 UTC 22 June, illustrated in Supporting Information, Analysis S1. This feature was located at 16.7 km, near 49°N, 156°E. The steering wind accounts reasonably for a direct connection between the active eruption and this layer. Evidence of this is contained in Supporting Information Figure S5 showing Hybrid Single-Particle Lagrangian Integrated Trajectory (HYSPLIT) forward trajectories (Stein et al., 2015) initialized at Raikoke at the time of the Horváth et al. (2021) 16.5 km injection pulse. This and the previously discussed line of evidence reveal the likely immediate injection of some volcanic material to heights exceeding 16 km.

M20 also promote simulated, ash-driven Raikoke-cloud heights between 20 and 22 km 4 days post eruption. They did not present any validating or contradictory observations. We are not aware of any other publications with validating observations. The Vernier et al. (2024) analysis of CALIOP daily Raikoke cloud height two weeks post eruption (their Figure 6), in agreement with our CALIOP analysis, is a strong indicator of a nearly nonvarying cloud top ∼16-17 km, well below M20's theorized upward transport. Hence, regardless of the composition of the Raikoke aerosol cloud, there appear to be no unequivocal observations in support of M20's ash-driven effect.

Wells et al. (2023) simulated Raikoke ash in a nudged climate-model simulation using mineral dust as a proxy and specifying an external mixture with sulfate droplets. The better agreement with aerosol observations between ash+SO_2 and SO_2-only forcing persisted throughout summer 2019, implying long-lasting residual "ash" on a hemispheric scale (e.g. their Figure 9). However, Boone et al. (2022), whose primary aim was to identify Raikoke aerosol composition throughout 2019 and 2020 using aerosol IR spectroscopy, found no signal of ash in ACE-FTS aerosol spectra. Rather, Boone et al. found only sulfate signals in the IR spectra throughout the entire "blanket" of Raikoke stratospheric aerosol sampled by ACE-FTS. This was the case for several ACE-FTS Raikoke-layer observations in the first half of July for which we requested confirmation. For reference, two examples of such volcanic aerosol layers are found in the following ACE occultations: 4 July, 47°N, 126°W and 11 July, 65°N, 53°W. Their finding puts into question Wells et al. (2023) suggestion of a long-lasting residual external mixture of ash and sulfate. Even an internal ash/sulfate blend may be called into question considering the likelihood that this would impart IR spectra also comprising a blend of absorption features.

In summary, neither M20, Wells et al. (2023), K22, nor any other publication of which we are aware present suitably robust observational evidence for appreciable ash

in the evolving Raikoke aerosol cloud as opposed to the sulfate-dominated interpretation we put forward.

4.2 Potential Relevance of Ash/sulfate Mixture

Even if the Raikoke SSACCs were sulfate-dominated, might a mixture involving ash be a factor in SSACC behavior? It is clear from the presentation in Section 3.1-3.3 that positive UVAI signals of Raikoke ash diminish entirely by 25 June, being immediately replaced by scattering aerosol index enhancements that persist for at least two weeks. Moreover, we report independent sulfate AOD features on 3 July (Figure 4), well after ash signals vanished. But as discussed above, previous publications expressed or implied a long-term ash influence on the overall Raikoke cloud or even specifically with respect to South SSACC (K22). It was shown by K22 that indications of non-spherical particles in the Raikoke cloud lingered but diminished within a month post eruption. Our presentation of depolarization ratio in Table 1, Figures 5, 7, 13, and Supporting Information Figures S2 and S7 reveals values consistent with ash dominance the first week post eruption in CALIOP's daytime examples ($41\% > \delta_{mean} > 28\%$), notably co-present with OMPS SAI signals. After that, daytime δ central tendency drops by roughly half. In nighttime CALIOP samples, central tendency δ values were generally $< 10\%$. Mean values declined and eventually met the median ($\delta < 5\%$). Volcanic ash generally imparts a 532 nm particulate and volume depolarization ratio exceeding $\sim$25% (e.g. Prata et al., 2017) while pure liquid sulfate is non-depolarizing. Prata et al. (2017), following O'Neill et al. (2012), used a depolarization ratio threshold of 20% to distinguish between "ash-rich" and "sulfate-rich" volcanic clouds. With respect to this criterion, the Raikoke aerosols were sulfate-dominated within days of the eruption and increasingly so as the SSACCs aged. This raises the question as to whether trace amounts of ash in the SSACC merit consideration for interpreting SSACC heating/lofting, addressed next.

The UVAI response to purely absorbing aerosol such as ash, dust, and smoke has received much more attention and modeling (e.g. Torres et al., 2020; de Graaf et al., 2005) than UVAI for purely scattering particles, like hydrometeors and liquid sulfates (de Graaf et al., 2005; Penning de Vries et al., 2009, 2014). However, de Graaf et al. (2005) lay out a firm theoretical basis for the opposite sign of the UVAI for purely scattering aerosols and cloud particles. Moreover, Penning de Vries et al. (2014), who applied their so-called SCattering Index (SCI; synonymous with negative UVAI) to the Nabro volcanic cloud in 2011, stated, "UVAI are very sensitive to absorbing particles, particularly if they are elevated, hence even a relatively small amount of ash would cause UVAI to increase to near zero, or even positive values." Figure 1 in Penning de Vries et al. (2009) adequately illustrates this conclusion, even for aerosol layers much lower than Raikoke's. The question then arises as to particulate mixtures, internal or external, of ash plus liquid sulfate and how they might influence UV scattering aerosol index.

To our knowledge, theoretical analysis of such conditions (e.g. sulfate-coated ash) has not been published. We can conclude from published literature on the absorbing aerosol index (positive AI values) that even trace amounts of absorbing aerosol at stratospheric altitudes impart a positive AI. This has been demonstrated in the cases of wildfire smoke and volcanic ash, wherein the clouds are traceable with positive AI for weeks. It was dramatically evident in the case of the Australia New Year pyroCb smoke cloud associated with compact anticyclonic circulations (Kablick et al., 2020; Khaykin et al., 2020) and Australia's Black Saturday (Allen et al., 2024). An excellent UTLS ash case demonstrating enduring positive UVAI is that of the Puyehue-Cordon Caulle ash cloud of 2011 (Carn & Krotkov, 2016).

Absorbing (i.e. positive) UVAI depends on 3 primary cloud qualities: altitude, aerosol optical depth, and single scatter albedo. Hence, the UVAI of a UTLS cloud clearly exhibiting strong optical depth is highly sensitive to its bulk single scatter albedo. This

is even the case for absorbing-aerosol-polluted ice clouds. Two noteworthy examples involve smoke/ice mixtures (e.g. Fromm et al., 2005) and the so-called dust-infused baroclinic storm (DIBS) cirrus shield, which contains a blend of cirrus ice and desert dust at the cloud top (Fromm et al., 2016). Such is the contribution of the absorbing-aerosol component that these icy cloud shields occasionally yield a positive UVAI rather than near zero UVAI for pure ice (de Graaf et al., 2005). It follows that a concentrated stratospheric aerosol layer exhibiting negative UVAI must have an effective single-scatter albedo near unity, regardless of the composition or details of the internal mixture within the particles such as sulfate-coated ash or any other absorbing particle type. Near-unity single-scatter albedo implies either the near absence of absorbing aerosol or an effective masking of the absorbing aerosol's sensitivity to incoming shortwave radiation. In either case the presence of a dense, stratospheric volcanic cloud with negative UVAI represents either the absence or inconsequential abundance of and absorption by ash. It is arguable also that after the scattering aerosol index signal vanishes, the ash fraction continues to decline (K22). Hence there is little support for an appreciable role of ash in SSACC composition and radiative performance. The foundational literature enables us to conclude with confidence that the sulfate-coated ash condition either does not manifest in the Raikoke cloud or that it is irrelevant if it does.

4.3 SSACC SO_2 as Proxy for Sulfate Concentration

The peak CALIOP AOD of the SSACC on 6 July studied in Section 3.4.1 (Figure 7) is within the range of the four samples reported in Table 1 for the younger Raikoke encounters. To the extent that these various CALIOP encounters with Raikoke SSACCs measure the focal features, it appears that the sulfate concentration is roughly non-varying out to two weeks post eruption. During this timeframe, the SSACC's integrated SO_2 mass declines appreciably and predictably, as detailed in Section 3.5. This curious situation be explained as a balance between leakage of primary sulfuric acid droplets from the SSACC (as inferred from filaments seen in the illustrated GOES and OMPS imagery) and secondary formation via gas-to-particle conversion. These observations may motivate deeper study into this and alternate explanations. So whereas individual snapshots of Raikoke SO_2 and aerosol concentration manifest a positive correlation within the volcanic cloud, the temporal correspondence between them is indicative of the expected gas-particle conversion. The OMPS scattering aerosol index diminishes somewhat between the values in Table 1 and 6 July (minimum: -2.6), but is still considerably enhanced. Further work is needed to understand all the factors determining the UV scattering aerosol index in an evolving stratospheric volcanic cloud.

4.4 Differential Diabatic Rise Between North and South SSACC

The diabatic rise of South SSACC has been thoroughly documented by Chouza et al. (2020), G21, C22, and K22. As reported herein, North SSACC's diabatic rise was appreciable but considerably less than that of South SSACC even though its AOD was on par with South SSACC for much of its life (Figure 18). A plausible distinction between North and South SSACC that could be a factor in the diabatic rise disparity is that North SSACC remained at middle and high latitudes throughout its existence, whereas South SSACC spent more than two months at subtropical latitudes where clear-sky surface temperatures are climatologically relatively great. This temperature differential would naturally provide greater thermal forcing on South SSACC, and thus naturally more absorption/heating potential. It is beyond the scope of this admittedly long paper to examine this satisfactorily but can be tested in follow-on work.

4.5 SSACC Depolarization Ratio Chronology

Utilizing all available CALIOP intercepts of the North and South SSACCs, it is apparent that there are steadily declining δ values. Again, we note the difference in SNR between nighttime and daytime CALIOP data that, if not considered, can skew the interpretation of δ values. In Supporting Information Figure S7, we show a chronology of mean and median δ values for Raikoke SSACC intercepts. Shown in the figure are the median (open circle), mean (closed circle) and the standard deviation about the mean (whiskers) for all observations (Figure S7a), daytime only (b), and nighttime only observations (c). The latter of which are almost all in Prata et al. (2017)'s category of "sulfate rich." We also draw attention to K22's Figure S6 and its ramifications for ash influence. Note that K22's Figure S6 shows that South SSACC's ash backscatter fraction at no point exceeds 50%; by their definition the SSACC is sulfate-dominated throughout that period and indisputably later on. Sulfate dominance exceeds 85% within one month of South SSACC's life. We note that CALIOP δ does not conform to a normal distribution, and the median (open circles) is a better statistic than the mean (closed circles) when making comparisons. Cf. the histograms in Figure S2.

The underpinning of K22's analysis is the work of Vernier et al. (2016), who implicitly treated ash as imparting a non-varying and strong depolarization consistent with its expected asphericity. I.e. they did not entertain any nuance of a sulfate/ash mixture that takes on a spherical condition. Absent that nuance, K22's results are totally consistent with our analysis.

4.6 Utility of GOES Imagery

The GOES images add value in three ways: 1. maps of volcanic aerosol augment our paper's—and previous publications'—reliance on SO_2 maps to track Raikoke-cloud evolution, 2. advantageous view conditions and temporal resolution as compared to polar-orbiter visible images, and 3. to show indications of contained circulation in animations. Visual circulation-detection cues are tenuous because angular velocities are small, especially soon after SSACC genesis. That said, we hold that marks of anticyclonic motion are subtly discernible in each visible and IR animation. We note that another clue, the filaments attached to the SSACCs, is a telltale indicator of leakage from a compact vortex. For example, see K22's Figure 1a and our Figure 9.

5 Conclusions

The Raikoke-generated stratospheric volcanic cloud manifested the curious occurrence of compact, persistent aerosol/SO_2 cloud elements, one of which rose diabatically roughly 10 km above injection altitude, according to a group of publications cited herein. A new revelation, that of internal anticyclonic circulation, was also previously reported (K22). K22 postulated that the diabatic ascent of their "vorticized volcanic plume" was due to internal heating resulting from absorption of incoming solar and reflected visible radiation by residual ash. Our study examined this cloud phenomenon, which we described as a sulfate/SO_2 anticyclonic contained circulation (SSACC) by introducing several lines of observational evidence characterizing the particulate composition and life cycle of two SSACCs.

IASI SO_2-concentration data were used to characterize the gaseous component of the Raikoke sulfur burden. The aerosol component of the SSACCs was documented with a combination of passive and active remote sensing, including OMPS-NM UV absorbing and scattering aerosol index, GOES imagery, MODIS visible reflectance and AOD, and CALIOP backscatter and depolarization data. It was found that SO_2 enhancements were accompanied by aerosols on every measurement occasion from the eruption onward. The OMPS UV data indicated an ash-dominated cloud top initially, followed within two

days post eruption by decay and replacement by scattering aerosol dominance. CALIOP depolarization ratio data qualitatively reflected the decay of ash presence, a minor residual of which was inferred by the MPLNET depolarization data of one of the SSACCs on 7 July over Alaska.

K22's finding of contained anticyclonic circulation within the SSACC was reinforced in two aspects of our analysis. First, several instances of GOES visible-reflectance animations of the SSACCs in favorable lighting conditions painted a picture of the omnipresence of circulating cloud-top material, starting as early as 24 June. Secondly, a novel combination of GOES visible imagery, MPLNET profiling, and stratospheric high-vertical-resolution radiosonde wind-direction and balloon-position data gave in situ proof of anomalous circulation precisely aligned with the vertical extent of the Raikoke SSACC. Radiosonde temperature data are of course also available for this profile, however reporting on that was beyond our intention and scope.

GOES window IR BT data, in combination with visible imagery, revealed a lasting association of terrestrial IR absorption within each SSACC. The implication we drew is that the retention of sulfate aerosols within the SSACCs presented an absorption cross section sufficient to intercept relatively warm terrestrial radiation and thereby modify the local SSACC footprint. However, it remains to be determined what compositional and microphysical properties could impart the thermal IR absorption reported herein. To that end, we have begun experiments with radiative transfer model simulations. Simulations and results of these experiments will be presented in a separate paper. Preliminary indications are that the model can produce brightness temperature anomalies within a month-old SSACC by computing the upwelling radiance at the top of the atmosphere (TOA; 100 km in the model) as viewed by GOES West (GOES 17) Channel 13 (10.3 μm) for the atmospheric conditions described in Section 3.6.3.

We contend that the observed diabatic lofting of both SSACCs was a consequence of this longwave heating. This is an alternative to K22's explanation of the diabatic heating being a consequence of shortwave absorption by residual ash particles. The geo-temporal evolution of the SSACC ascent we illustrated did not comport with K22's finding of influence by the cloudy conditions associated with the Asian monsoon convection.

The canonical model of volcanic SO_2-to-sulfate conversion Robock (2000) is belied by the evidence presented herein. We showed that sulfate-dominated AOD was a feature of the Raikoke stratospheric volcanic cloud from its nascent stage. These "young" sulfates are not a new observation (Guo et al., 2004; Fromm et al., 2013; Penning de Vries et al., 2014). They have been recognized as a noteworthy contributor to fresh stratospheric volcanic clouds such as that generated by the 2022 eruption of Hunga Tonga–Hunga Ha'apai volcano (e.g. Boichu et al. (2023)). The unified UV scattering aerosol index, AOD (CALIOP and MODIS), and GOES visible reflectance indicate a strong, early sulfate presence in the Raikoke volcanic cloud. It is therefore incumbent on the research community to survey all stratospheric volcanic clouds in the satellite era for the purpose of quantifying the total sulfur burden, gaseous and particulate.

If indeed the Raikoke SSACCS' sulfate burden and microphysics were sufficient to locally perturb stratospheric thermal structure, it is reasonable to extrapolate that the overall Raikoke volcanic cloud presented a radiative shield in proportion to the cloud's AOD. This would suggest the potential for a larger, continental/hemispheric perturbation to the stratospheric thermal background during the months-long AOD decay. This is a subject so far unexplored to our knowledge yet worthy of future exploration. It has been previously established that the Pinatubo sulfate cloud generated a year-long IR absorption phenomenon (Labitzke & McCormick, 1992) that apparently was the cause for erroneous sea-surface temperature retrievals derived from satellite IR data (Reynolds, 1993). We propose that the Raikoke stratospheric sulfate cloud offers a new opportu-

nity for examination of such an impact appropriately scaled to the Raikoke sulfate abundance and decay.

The injection of SO_2 into the stratosphere has been proposed as a technique for geoengineering the Earth's climate (Crutzen, 2006; Shepherd, 2009). Considerable effort has focused on the large scale climate impacts of the release of SO_2 (e.g. Laakso et al., 2022; Weisenstein et al., 2022). The evolution of the two SSACCs provide excellent case studies to test models of sulfuric acid formation and development in the stratosphere. Given the unexpected longevity of the SSACCS, microphysical studies are needed to improve confidence in the predicted environmental impact of this method of geoengineering.

Finally, we acknowledge reporting by Legras et al. (2022) of discrete stratospheric sulfate cloud elements after the eruption of Hunga Tonga–Hunga Ha'apai volcano in January 2022 that bore a resemblance to the Raikoke SSACCs. These more recent sulfate cloud elements were much greater in size compared to those formed after Raikoke, but Legras et al. presented evidence of sheared motion within one of them. Naturally, further exploration of this and other volcanic clouds with the aim of finding similarities in compact, persistent sulfate clouds should be a high priority.

Conflicts of Interest

The authors declare no conflicts of interest relevant to this study.

Open Research Section

Data Availability Statement

The IASI SO_2 outputs will be maintained by the Earth Observation Data Group for the next five years and can be made available on request subject to the AGU data availability guidelines (University of Oxford Earth Observation Data Group, 2025). OMPS-NM level 2 UV aerosol index data are available from the NASA Goddard Earth Sciences (GES) Data and Information Services Center (DISC, 2025). CALIOP data are available from the EarthData Atmospheric Science Data Center (ASDC, 2025). MPLNET data reside and are downloadable from the repository hosted by Goddard Space Flight Center (GSFC, MPLNET, 2025). GOES data are stored within the Amazon Web Services repository, which is accessed via NOAA's Weather and Climate Toolkit at the National Center for Environmental Information (NCEI, 2025b). High vertical resolution radiosonde data are also accessible at NOAA's NCEI (NCEI, 2025a). Data for Figure 4 are available (JASMIN, 2025), and more information about and visualized products from the Rutherford Appleton Laboratory Remote Sensing Group are also available (RAL, 2025).

Acknowledgments

We thank Robert Levy for his assistance with the calculation of MODIS AOD for the special circumstances of our 6 July 2019 case. We acknowledge Chris Boone for his clarifications regarding ACE-FTS Raikoke ash detection. IAT and RGG are grateful for the support of the NERC Centre for the Observation and Modelling of Earthquakes, Volcanoes and Tectonics (COMET), a partnership between UK Universities and the British Geological Survey. They are also grateful to the National Centre for Earth Observation (NCEO) and the Leverhulme Trust who helped facilitate this study. IAT and RGG were funded through the Natural Environment Research Council (NERC) project VPLUS (NE/S004025/1). Additionally, RGG was supported by the NERC project R4-Ash (NE/S003843/1). We are grateful to EUMETSAT for the provision of the IASI level 1c data and to ECMWF for the meteorological data used in the IASI SO_2 retrievals. These datasets were accessed at the Centre for Environmental Data Analysis (CEDA, EUMETSAT, 2009, 2014, 2021; European Centre for Medium-Range Weather Forecasts, 2012). The MPLNET project is funded by the NASA Radiation Sciences Program and the Earth Observing System.

References

Allen, D. R., Fromm, M. D., Kablick III, G. P., & Nedoluha, G. E. (2020). Smoke with Induced Rotation and Lofting (SWIRL) in the Stratosphere. *Journal of the Atmospheric Sciences*, *77*, 4297-4316. doi: 10.1175/JAS-D-20-0131.1

Allen, D. R., Fromm, M. D., Kablick III, G. P., Nedoluha, G. E., & Peterson, D. A. (2024). Smoke with Induced Rotation and Lofting (SWIRL) Generated by the February 2009 Australian Black Saturday PyroCb Plume. *J. Geophys. Res. Atmos.*, *129*(5), e2023JD040289. doi: https://doi.org/10.1029/2023JD040289

ASDC. (2025). CALIOP Level 1 Data [Dataset]. doi: https://doi:10.5067/CALIOP/CALIPSO/CAL_LID_L1-Standard-V4-51

Blumstein, D., Chalon, G., Carlier, T., Buil, C., Hebert, P., Maciaszek, T., ... others (2004). IASI instrument: Technical overview and measured performances. *Infr. Spaceborne Rem. Sens. XII*, *5543*, 196–207.

Boichu, M., Grandin, R., Blarel, L., Torres, B., Derimian, Y., Goloub, P., ... Riedi, J. (2023). Growth and Global Persistence of Stratospheric Sulfate Aerosols From the 2022 Hunga Tonga–Hunga Ha'apai Volcanic Eruption. *J. Geophys. Res. Atmos.*, *128*(23), e2023JD039010.

Boone, C. D., Bernath, P. F., Labelle, K., & Crouse, J. (2022). Stratospheric Aerosol Composition Observed by the Atmospheric Chemistry Experiment Following the 2019 Raikoke Eruption. *J. Geophys. Res. Atmos.*, *127*. doi: 10.1029/2022JD036600

Cai, Z., Griessbach, S., & Hoffmann, L. (2022). Improved estimation of volcanic SO_2; injections from satellite retrievals and Lagrangian transport simulations: the 2019 Raikoke eruption. *Atmos. Chem. Phys.*, *22*, 6787-6809. doi: 10.5194/acp-22-6787-2022

Cameron, W. D., Bernath, P., & Boone, C. (2021). Sulfur dioxide from the atmospheric chemistry experiment (ACE) satellite. *J. Quant. Spectros. Ra.*, *258*, 107341. doi: 10.1016/j.jqsrt.2020.107341

Campbell, J. R., Hlavka, D. L., Welton, E. J., Flynn, C. J., Turner, D. D., Spinhirne, J. D., ... Hwang, I. (2002). Full-time, eye-safe cloud and aerosol lidar observation at atmospheric radiation measurement program sites: Instruments and data processing. *J. Atmos. Ocean. Tech.*, *19*(4), 431–442. doi: https://doi.org/10.1175/1520-0426(2002)019\%3C0431:FTESCA\%3E2.0.CO;2

Carboni, E., Grainger, R., Walker, J., Dudhia, A., & Siddans, R. (2012). A new scheme for sulphur dioxide retrieval from IASI measurements: application to the Eyjafjallajökull eruption of April and May 2010. *Atmos. Chem. Phys.*, *12*(23), 11417-11434. doi: 10.5194/acp-12-11417-2012

Carboni, E., Grainger, R. G., Mather, T. A., Pyle, D. M., Thomas, G. E., Siddans, R., ... Balis, D. (2016). The vertical distribution of volcanic SO_2 plumes measured by IASI. *Atmos. Chem. Phys.*, *16*, 4343-4367. doi: 10.5194/acp-16-4343-2016

Carboni, E., Mather, T. A., Schmidt, A., Grainger, R. G., Pfeffer, M. A., Ialongo, I., & Theys, N. (2019). Satellite-derived sulfur dioxide (SO_2) emissions from the 2014–2015 Holuhraun eruption (Iceland). *Atmos. Chem. Phys.*, *19*(7), 4851–4862. doi: 10.5194/acp-19-4851-2019

Carn, S., Clarisse, L., & Prata, A. (2016). Multi-decadal satellite measurements of global volcanic degassing. *J. Volcanol. and Geoth. Res.*, *311*, 99-134. doi: 10.1016/j.jvolgeores.2016.01.002

Carn, S., & Krotkov, N. (2016). *Ultraviolet satellite measurements of volcanic ash.* Elsevier. doi: 10.1016/B978-0-08-100405-0.00018-5

Chouza, F., Leblanc, T., Barnes, J., Brewer, M., Wang, P., & Koon, D. (2020). Long-term (1999–2019) variability of stratospheric aerosol over Mauna Loa, Hawaii, as seen by two co-located lidars and satellite measurements. *Atmos. Chem. Phys.*, *20*, 6821-6839. doi: 10.5194/acp-20-6821-2020

Clerbaux, C., Boynard, A., Clarisse, L., George, M., Hadji-Lazaro, J., Herbin, H., ... Coheur, P.-F. (2009). Monitoring of atmospheric composition using the thermal infrared IASI/MetOp sounder. *Atmos. Chem. Phys.*, *9*(16), 6041-6054. doi: 10.5194/acp-9-6041-2009

Crafford, A., & Venzke, E. (2019). *Global Volcanism Program, 2019. Report on Raikoke (Russia)* (Tech. Rep.). Bulletin of the Global Volcanism Network, 44:8, Smithsonian Institution. Retrieved from `https://volcano.si.edu/showreport.cfm?doi=10.5479/si.GVP.BGVN201908-290250` doi: https://doi.org/10.5479/si.GVP.BGVN201908-290250

Crutzen, P. J. (2006). Albedo enhancement by stratospheric sulfur injections: A contribution to resolve a policy dilemma? *Climatic Change*, *77*(3-4), 211. doi: https://doi.org/10.1007/s10584-006-9101-y

de Graaf, M., Stammes, P., Torres, O., & Koelemeijer, R. B. A. (2005). Absorbing Aerosol Index: Sensitivity analysis, application to GOME and comparison with TOMS. *J. Geophys. Res. Atmos.*, *110*(D1). doi: https://doi.org/10.1029/2004JD005178

de Leeuw, J., Schmidt, A., Witham, C. S., Theys, N., Taylor, I. A., Grainger, R. G., ... Kristiansen, N. I. (2021). The 2019 Raikoke volcanic eruption–Part 1: Dispersion model simulations and satellite retrievals of volcanic sulfur dioxide. *Atmos. Chem. Phys.*, *21*, 10851-10879. doi: 10.5194/acp-21-10851-2021

DISC. (2025). OMPS-NM Level 2 UV Aerosol Index Data [Dataset]. doi: https://doi.org/10.5067/40L92G8144IV

EUMETSAT. (2009). *IASI atmospheric spectra (L1C product) from the EPS Metop-A satellite: CEDA mirror archive for STFC, NCAS, NCEO. EUMETSAT.* `https://catalogue.ceda.ac.uk/uuid/ea46600afc4559827f31dbfbb8894c2e`. (Accessed: 2024-03-18)

EUMETSAT. (2014). *IASI atmospheric spectra (L1C product) from the EPS Metop-B satellite: CEDA mirror archive for STFC, NCAS, NCEO. NERC Earth Observation Data Centre.* `https://catalogue.ceda.ac.uk/uuid/0092c4fe29f76c1b99b4dc19133f361a`. (Accessed: 2024-03-18)

EUMETSAT. (2021). *IASI atmospheric spectra (L1C product) from the EPS Metop - C satellite: CEDA mirror archive for STFC, NCAS, NCEO. EUMETSAT.* `https://catalogue.ceda.ac.uk/uuid/58648f7210c84c44a91dc128d8d750d8`. (Accessed: 2024-03-18)

European Centre for Medium-Range Weather Forecasts. (2012). *ECMWF Operational Regular Gridded Data at 1.125 degrees resolution. NCAS British Atmospheric Data Centre.* `https://catalogue.ceda.ac.uk/uuid/a67f1b4d9db7b1528b800ed48198bdac`. (Accessed: 2024-03-18)

Fromm, M., Bevilacqua, R., Servranckx, R., Rosen, J., Thayer, J. P., Herman, J., & Larko, D. (2005). Pyro-cumulonimbus injection of smoke to the stratosphere: Observations and impact of a super blowup in northwestern Canada on 3–4 August 1998. *J. Geophys. Res. Atmos.*, *110*(D8). doi: https://doi.org/10.1029/2004JD005350

Fromm, M., Kablick, G., & Caffrey, P. (2016). Dust-infused baroclinic cyclone storm clouds: The evidence, meteorology, and some implications. *Geophys. Res. Lett.*, *43*. doi: 10.1002/2016GL071801

Fromm, M., Kablick, G., Nedoluha, G., Carboni, E., Grainger, R., Campbell, J., & Lewis, J. (2014). Correcting the record of volcanic stratospheric aerosol impact: Nabro and Sarychev Peak. *J. Geophys. Res. Atmos.*, *119*, 10,343-10,364. doi: 10.1002/2014JD021507

Fromm, M., Lindsey, D. T., Servranckx, R., Yue, G., Trickl, T., Sica, R., ... Godin-Beekmann, S. (2010). The Untold Story of Pyrocumulonimbus. *B. Amer. Meteorol. Soc.*, *91*, 1193-1210. doi: 10.1175/2010BAMS3004.1

Fromm, M., Nedoluha, G., & Charvát, Z. (2013). Comment on "Large Volcanic Aerosol Load in the Stratosphere Linked to Asian Monsoon Transport". *Science*, *339*, 647. doi: 10.1126/science.1228605

Gao, B.-C., & Kaufman, Y. J. (1995). Selection of the 1.375-µm MODIS Channel for Remote Sensing of Cirrus Clouds and Stratospheric Aerosols from Space. *J. Atmos. Sci.*, *52*, 4231-4237. doi: 10.1175/1520-0469(1995)052⟨4231:SOTMCF⟩2.0.CO;2

Geller, M. A., Wang, L., Chun, H.-Y., & Love, P. T. (2017). *Fine-scale atmospheric processes and structures.*

Gorkavyi, N., Krotkov, N., Li, C., Lait, L., Colarco, P., Carn, S., ... Joiner, J. (2021). Tracking aerosols and so2 clouds from the raikoke eruption: 3d view from satellite observations. *Atmos. Meas. Tech.*, *14*, 7545-7563. doi: 10.5194/amt-14-7545-2021

Guo, S., Bluth, G. J., Rose, W. I., Watson, I. M., & Prata, A. J. (2004). Re-evaluation of SO_2 release of the 15 June 1991 Pinatubo eruption using ultraviolet and infrared satellite sensors. *Geochem. Geophys. Geosy.*, *5*. doi: 10.1029/2003GC000654

Herman, J. R., Bhartia, P. K., Torres, O., Hsu, C., Seftor, C., & Celarier, E. (1997). Global distribution of UV-absorbing aerosols from Nimbus 7/TOMS data. *J. Geophys. Res. Atmos.*, *102*(D14), 16911-16922. doi: https://doi.org/10.1029/96JD03680

Holben, B., Eck, T., Slutsker, I., Tanré, D., Buis, J., Setzer, A., ... Smirnov, A. (1998). AERONET—A Federated Instrument Network and Data Archive for Aerosol Characterization. *Rem. Sens. Environ.*, *66*(1), 1-16. doi: https://doi.org/10.1016/S0034-4257(98)00031-5

Horváth, Á., Girina, O. A., Carr, J. L., Wu, D. L., Bril, A. A., Mazurov, A. A., ... Buehler, S. A. (2021). Geometric estimation of volcanic eruption column height from GOES-R near-limb imagery–Part 2: Case studies. *Atmos. Chem. Phys.*, *21*(16), 12207–12226. doi: 10.5194/acp-21-12207-2021

JASMIN. (2025). IMS-Aerosol H_2SO_4 AOD [Dataset]. Retrieved from `https://gws-access.jasmin.ac.uk/public/rsg_share/transfer/ims/eocis_l3/l3u/v1000/metopb/2019/`

Kablick, G. P., Allen, D. R., Fromm, M. D., & Nedoluha, G. E. (2020). Australian PyroCb Smoke Generates Synoptic-Scale Stratospheric Anticyclones. *Geophys. Res. Lett.*, *47*. doi: 10.1029/2020GL088101

Khaykin, S., de Laat, A. T. J., Godin-Beekmann, S., Hauchecorne, A., & Ratynski, M. (2022). Unexpected self-lofting and dynamical confinement of volcanic plumes: the Raikoke 2019 case. *Sci. Rep.*, *12*, 22409. doi: 10.1038/s41598-022-27021-0

Khaykin, S., Legras, B., Bucci, S., Sellitto, P., Isaksen, L., Tencé, F., ... Godin-Beekmann, S. (2020). The 2019/20 Australian wildfires generated a persistent smoke-charged vortex rising up to 35 km altitude. *Commun. Earth Environ.*, *1*, 22. doi: 10.1038/s43247-020-00022-5

Kloss, C., Berthet, G., Sellitto, P., Ploeger, F., Taha, G., Tidiga, M., ... Legras, B. (2021). Stratospheric aerosol layer perturbation caused by the 2019 Raikoke and Ulawun eruptions and their radiative forcing. *Atmos. Chem. Phys.*, *21*, 535-560. doi: 10.5194/acp-21-535-2021

Knepp, T. N., Thomason, L., Kovilakam, M., Tackett, J., Kar, J., Damadeo, R., & Flittner, D. (2022). Identification of smoke and sulfuric acid aerosol in SAGE III/ISS extinction spectra. *Atmos. Meas. Tech.*, *15*, 5235-5260. doi: 10.5194/amt-15-5235-2022

Ko, H., Chun, H., Wilson, R., & Geller, M. A. (2019). Characteristics of Atmospheric Turbulence Retrieved From High Vertical-Resolution Radiosonde Data in the United States. *J. Geophys. Res. Atmos.*, *124*, 7553-7579. doi: 10.1029/2019JD030287

Laakso, A., Niemeier, U., Visioni, D., Tilmes, S., & Kokkola, H. (2022). Dependency of the impacts of geoengineering on the stratospheric sulfur injection strategy– Part 1: Intercomparison of modal and sectional aerosol modules. *Atmos. Chem. Phys.*, *22*(1), 93–118. doi: https://doi.org/10.5194/acp-22-93-2022

Labitzke, K., & McCormick, M. P. (1992). Stratospheric temperature increases due to pinatubo aerosols. *Geophys. Res. Lett.*, *19*, 207-210. doi: 10.1029/91GL02940

Labitzke, K., Naujokat, B., & McCormick, M. P. (1983). Temperature effects on the stratosphere of the April 4, 1982 eruption of El Chichón, Mexico. *Geophys. Res. Lett.*, *10*, 24-26. doi: 10.1029/GL010i001p00024

Legras, B., Duchamp, C., Sellitto, P., Podglajen, A., Carboni, E., Siddans, R., ... Ploeger, F. (2022). The evolution and dynamics of the Hunga Tonga–Hunga Ha'apai sulfate aerosol plume in the stratosphere. *Atmos. Chem. Phys.*, *22*(22), 14957–14970. doi: 10.5194/acp-22-14957-2022

Lestrelin, H., Legras, B., Podglajen, A., & Salihoglu, M. (2021). Smoke-charged vortices in the stratosphere generated by wildfires and their behaviour in both hemispheres: Comparing Australia 2020 to Canada 2017. *Atmos. Chem. Phys.*, *21*. doi: 10.5194/acp-21-7113-2021

Love, P. T., & Geller, M. A. (2013). Exploring and Improving Access to High Vertical Resolution Radiosonde Data. *Eos*, *94*, 401-401. doi: 10.1002/2013EO440006

MPLNET. (2025). Micropulse Lidar Network Data [Dataset]. Retrieved from `https://mplnet.gsfc.nasa.gov/download_tool/`

Muser, L. O., Hoshyaripour, G. A., Bruckert, J., Horváth, A., Malinina, E., Wallis, S., ... Vogel, B. (2020). Particle aging and aerosol–radiation interaction affect volcanic plume dispersion: evidence from the Raikoke 2019 eruption. *Atmos. Chem. Phys.*, *20*, 15015-15036. doi: 10.5194/acp-20-15015-2020

NCEI. (2025a). High Vertical Resolution Radiosonde Data [Dataset]. Retrieved from `https://www.ncei.noaa.gov/data/us-radiosonde-bufr/archive/`

NCEI. (2025b). NOAA Weather and Climate Toolkit [Dataset]. Retrieved from `https://www.ncdc.noaa.gov/wct/`

O'Neill, N. T., Perro, C., Saha, A., Lesins, G., Duck, T. J., Eloranta, E. W., ... Savastiouk, V. (2012). Properties of Sarychev sulphate aerosols over the Arctic. *J. Geophys. Res. Atmos.*, *117*(D4). doi: https://doi.org/10.1029/2011JD016838

Osborne, M. J., de Leeuw, J., Witham, C., Schmidt, A., Beckett, F., Kristiansen, N., ... Haywood, J. (2022). The 2019 Raikoke volcanic eruption – Part 2: Particle-phase dispersion and concurrent wildfire smoke emissions. *Atmos. Chem. Phys.*, *22*, 2975-2997. doi: 10.5194/acp-22-2975-2022

Penning de Vries, M. J. M., Beirle, S., & Wagner, T. (2009). UV Aerosol Indices from SCIAMACHY: introducing the SCattering Index (SCI). *Atmos. Chem. Phys.*, *9*, 9555-9567. doi: 10.5194/acp-9-9555-2009

Penning de Vries, M. J. M., Dörner, S., Puķīte, J., Hörmann, C., Fromm, M. D., & Wagner, T. (2014). Characterisation of a stratospheric sulfate plume from the nabro volcano using a combination of passive satellite measurements in nadir and limb geometry. *Atmos. Chem. Phys.*, *14*, 8149-8163. doi: 10.5194/acp-14-8149-2014

Prata, A. T., Grainger, R. G., Taylor, I. A., Povey, A. C., Proud, S. R., & Poulsen, C. A. (2022). Uncertainty-bounded estimates of ash cloud properties using the ORAC algorithm: application to the 2019 Raikoke eruption. *Atmos. Meas. Tech.*, *15*, 5985-6010. doi: 10.5194/amt-15-5985-2022

Prata, A. T., Young, S. A., Siems, S. T., & Manton, M. J. (2017). Lidar ratios of stratospheric volcanic ash and sulfate aerosols retrieved from CALIOP measurements. *Atmos. Chem. Phys.*, *17*(13), 8599–8618. doi: 10.5194/acp-17-8599-2017

RAL. (2025). Rutherford Appleton Laboratory Remote Sensing Group [Dataset]. Retrieved from `https://www.ralspace.stfc.ac.uk/Pages/Remote-Sensing.aspx`

Remer, L. A., Levy, R. C., Mattoo, S., Tanré, D., Gupta, P., Shi, Y., ... Holben, B. N. (2020). The dark target algorithm for observing the global aerosol system: Past, present, and future. *Remote Sens.*, *12*, 2900. doi: 10.3390/rs12182900

Reynolds, R. W. (1993). Impact of Mount Pinatubo Aerosols on Satellite-derived Sea Surface Temperatures. *J. Climate*, *6*, 768-774. doi: 10.1175/1520-0442(1993)006⟨0768:IOMPAO⟩2.0.CO;2

Robock, A. (2000). Volcanic eruptions and climate. *Rev. Geophys.*, *38*(2), 191–219. doi: https://doi.org/10.1029/1998RG000054

Rose, W. I., Gu, Y., Watson, I. M., Yu, T., Blut, G. J. S., Prata, A. J., ... Flittner, D. E. (2003). *The february–march 2000 eruption of hekla, iceland from a satellite perspective* (Vol. 139). AGU American Geophysical Union. doi: 10.1029/139GM07

Schmit, T. J., Griffith, P., Gunshor, M. M., Daniels, J. M., Goodman, S. J., & Lebair, W. J. (2017). A Closer Look at the ABI on the GOES-R Series. *B. Amer. Meteorol. Soc.*, *98*, 681-698. doi: 10.1175/BAMS-D-15-00230.1

Shepherd, J. G. (2009). *Geoengineering the climate: science, governance and uncertainty*. Royal Society.

Stein, A. F., Draxler, R. R., Rolph, G. D., Stunder, B. J., Cohen, M. D., & Ngan, F. (2015). Noaa's hysplit atmospheric transport and dispersion modeling system. *B. Amer. Meteorol. Soc.*, *96*(12), 2059–2077. doi: https://doi.org/10.1175/BAMS-D-14-00110.1

Torres, O., Jethva, H., Ahn, C., Jaross, G., & Loyola, D. G. (2020). TROPOMI aerosol products: Evaluation and observations of synoptic-scale carbonaceous aerosol plumes during 2018-2020. *Atmos. Meas. Tech.*, *13*, 6789-6806. doi: 10.5194/amt-13-6789-2020

University of Oxford Earth Observation Data Group. (2025). IASI SO_2 maintained by the Earth Observation Data Group [Dataset]. Retrieved from `http://eodg.atm.ox.ac.uk/eodg/`

Vaughan, M., Winker, D., & Powell, K. (2005). Part 2: Feature Detection and Layer Properties Algorithms. In *CALIOP Algorithm Theoretical Basis Document* (p. 87 pp.). Langley Research Center, Hampton, VA. Retrieved from `http://www-calipso.larc.nasa.gov/resources/pdfs/PC-SCI-202_Part2_rev1x01.pdf`

Vernier, J.-P., Fairlie, T., Deshler, T., Natarajan, M., Knepp, T., Foster, K., ... Trepte, C. (2016). In situ and space-based observations of the Kelud volcanic plume: The persistence of ash in the lower stratosphere. *J. Geophys. Res. Atmos.*, *121*(18), 11–104. doi: https://doi.org/10.1002/2016JD025344

Walker, J., Carboni, E., Dudhia, A., & Grainger, R. (2012). Improved detection of sulphur dioxide in volcanic plumes using satellite-based hyperspectral infrared measurements: Application to the Eyjafjallajökull 2010 eruption. *J. Geophys. Res. Atmos.*, *117*(D20). doi: 10.1029/2011JD016810

Walker, J., Dudhia, A., & Carboni, E. (2011). An effective method for the detection of trace species demonstrated using the MetOp Infrared Atmospheric Sounding Interferometer. *Atmos. Meas. Tech.*, *4*, 1567–1580. doi: 10.5194/amt-4-1567-2011

Walton, C. (1985). Satellite Measurement of Sea Surface Temperature in the Presence of Volcanic Aerosols. *J. Clim. Appl. Meteorol.*, *24*, 501-507. doi: 10.1175/1520-0450(1985)024⟨0501:SMOSST⟩2.0.CO;2

Weisenstein, D. K., Visioni, D., Franke, H., Niemeier, U., Vattioni, S., Chiodo, G., ... Keith, D. W. (2022). An interactive stratospheric aerosol model intercomparison of solar geoengineering by stratospheric injection of SO_2 or accumulation-mode sulfuric acid aerosols. *Atmos. Chem. Phys.*, *22*(5), 2955–2973. doi: https://doi.org/10.5194/acp-22-2955-2022

Wells, A. F., Jones, A., Osborne, M., Damany-Pearce, L., Partridge, D. G., & Haywood, J. M. (2023). Including ash in UKESM1 model simulations of the Raikoke volcanic eruption reveals improved agreement with observations. *Atmos. Chem.*

Phys., *23*(7), 3985–4007. doi: 10.5194/acp-23-3985-2023

Welton, E. J., & Campbell, J. R. (2002). Micropulse lidar signals: Uncertainty analysis. *J. Atmos. Ocean. Tech.*, *19*(12), 2089–2094. doi: https://doi.org/10.1175/1520-0426(2002)019%3C2089:MLSUA%3E2.0.CO;2

Welton, E. J., Campbell, J. R., Spinhirne, J. D., & III, V. S. S. (2001). Global monitoring of clouds and aerosols using a network of micropulse lidar systems. In U. N. Singh, T. Itabe, & N. Sugimoto (Eds.), (p. 151). doi: 10.1117/12.417040

Welton, E. J., Stewart, S. A., Lewis, J. R., Belcher, L. R., Campbell, J. R., & Lolli, S. (2018). Status of the NASA Micro Pulse Lidar Network (MPLNET): overview of the network and future plans, new version 3 data products, and the polarized MPL. In *EPJ Web of Conferences* (Vol. 176, p. 09003). doi: https://doi.org/10.1051/epjconf/201817609003

Winker, D., Vaughan, M., Omar, A., Hu, Y., Powell, K., Liu, Z., ... Young, S. (2009). Overview of the CALIPSO mission and CALIOP data processing algorithms. *J. Atmos. Ocean. Tech.*, *26*(11), 2310–2323. doi: 10.1175/2009JTECHA1281.1

Table 1. Selected CALIOP aerosol, OMPS scattering aerosol index (SAI), and IASI SO_2 metrics of localized Raikoke cloud sub-elements, 23 June–1 July 2019. See Figure 3 for mapped markers of the CALIPSO orbit segment, IASI, and OMPS pixel locations. Time in UTC is provided in Supporting Information Table S1. All CALIOP observations are daytime orbit segments to better temporally match IASI.

	CALIOP								OMPS			IASI		
Date	AOD_{max}	AOD_{mean}	z_{max}	θ_{max}	z_{mean}	θ_{mean}	δ_{mean}	δ_{median}	SAI	Lat. (°N)	Lon. (°E)	SO_2(DU)	Lat. (°N)	Lon. (°E)
23 June	13.7	0.3	13.5	379	12.9	371	0.41	0.35	-5.7	49.1	175.4	75.5	48.2	174.7
25 June	5.8	0.2	13.8	392	13.2	382	0.41	0.33	-2.9	56.3	177.6	93.2	56.8	180.5
29 June	4.9	0.2	15.2	415	14.2	395	0.27	0.19	-4.9	58.1	138.6	79.7	59.6	137.0
01 July	6.5	0.3	15.5	414	14.5	399	0.28	0.19	-3.3	53.5	146.8	70.7	54.0	144.3

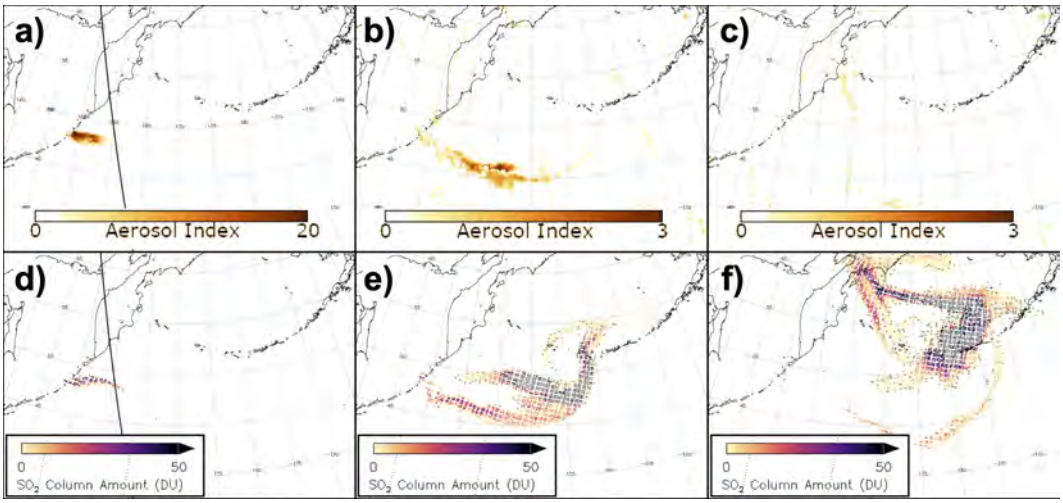

Figure 1. Raikoke aerosol and SO_2 cloud, 22-24 June 2019. OMPS positive UVAI, panels (a)-(c). Note the variable color scaling for each day. Panels (d)-(f), IASI descending SO_2 concentration in Dobson Units (DU) from the iterative retrieval run in its standard configuration for the full cloud (see Section 2), with a fixed color scale. The gray pixels have been flagged as containing elevated amounts of SO_2 by the linear retrieval but which do not pass the iterative retrieval quality control. UTC for (a)–(c): 22 June 03:09, 23 June 01:08, 24 June 02:30. UTC for (d)-(f): 21 June 22:09, 22 June 22:42, 23 June 23:07.

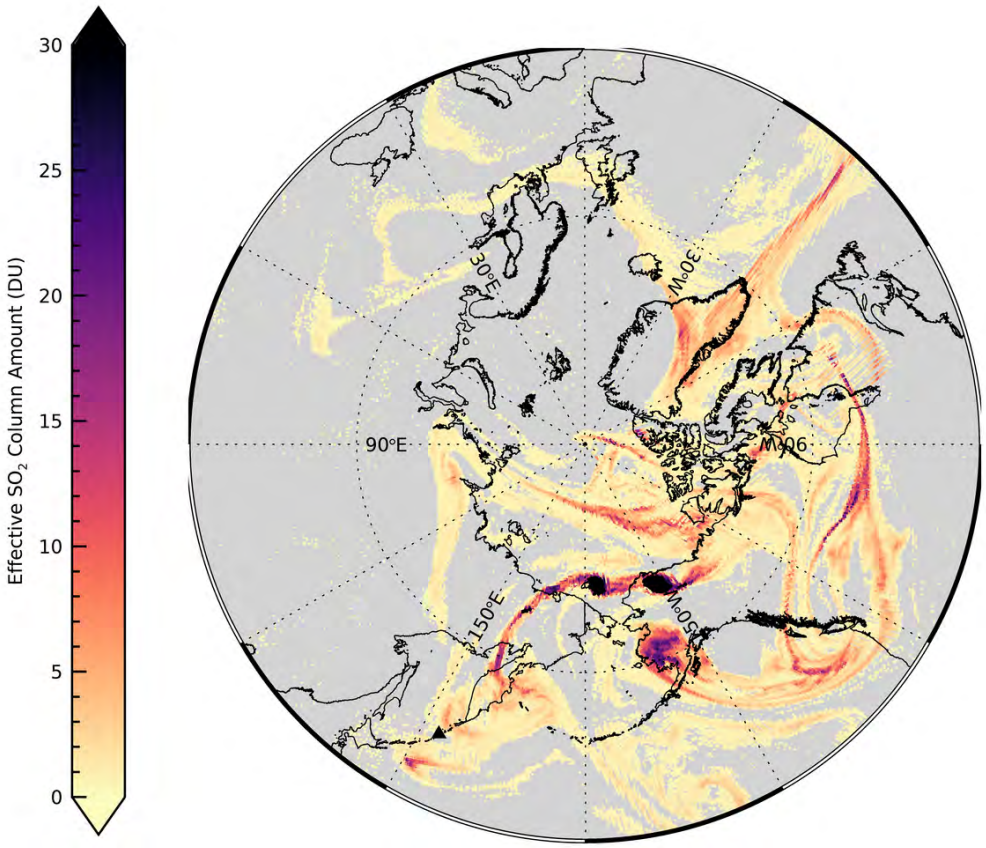

Figure 2. Overall Raikoke SO_2 on 6 July 2019. IASI SO_2 from the linear retrieval on this polar projection shows the full extent of the SO_2 cloud range two weeks post eruption.

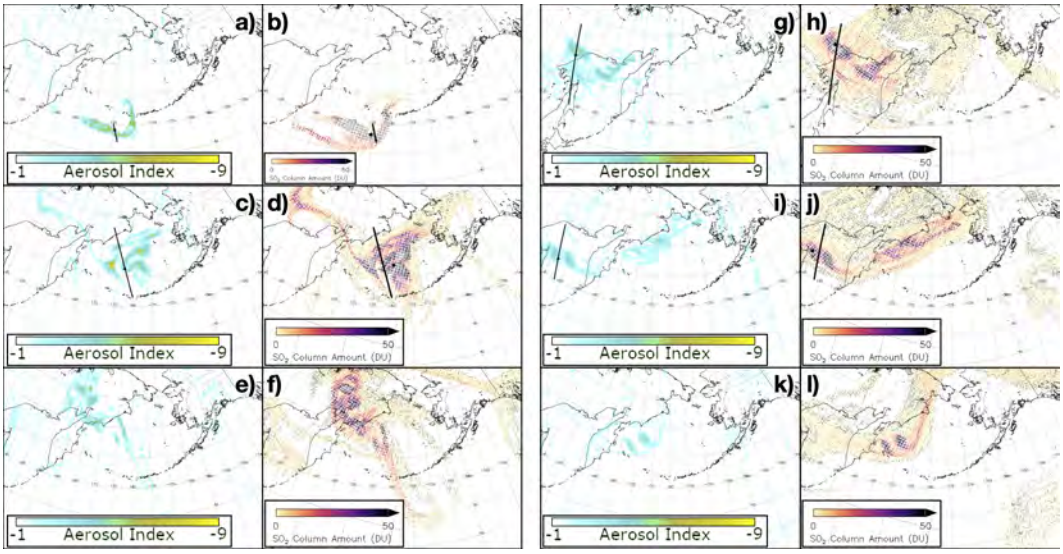

Figure 3. Initial evolution of Raikoke sulfate cloud: 23, 25, 27, 29 June, 1, 3 July NOAA 20 OMPS UV scattering index (i.e. negative values only) (panels a, c, e, g, i, k), and IASI descending SO_2 from the iterative retrieval (panels b, d, f, h, j, l); CALIPSO orbit segments applicable to Figure 5 are overlain on relevant panels (Black triangles in a, c, g, i; and black diamonds in b, d, h, j show the locations for Table 1). Gray pixels have been flagged as containing elevated amounts of SO_2 by the linear retrieval but which do not pass the iterative retrieval quality control. UTC for IASI panels (b,d,f,h,j,l): 22 June 22:09, 24 June 22:17, 26 June 22:12, 28 June 22:10, 30 June 22:29, 02 July 22:37. UTC for OMPS panels (a,c,e,g,I,k): 23 June 01:08 , 25 June 02:14 25, 27 June 01:39, 29 June 04:21, 01 July 03:42, 03 July 01:23.

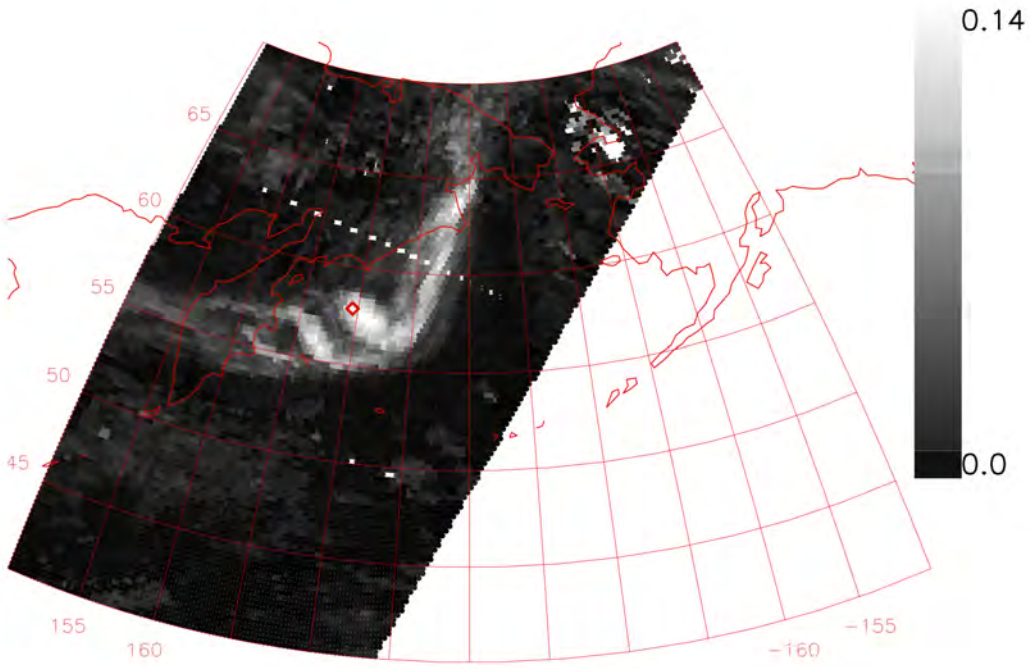

Figure 4. IMS-Aerosol H_2SO_4 AOD for daytime 3 July 2019. See the color bar for the AOD range displayed. The bold red diamond shows the location of the maximum AOD for this scene: 0.132.

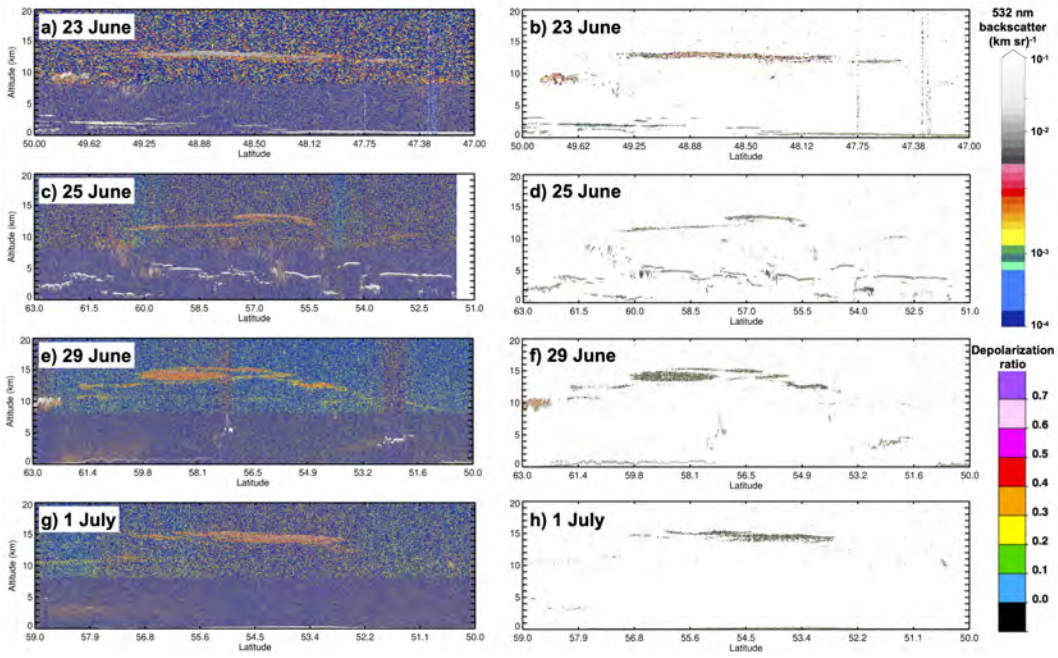

Figure 5. CALIOP 532 nm attenuated backscatter coefficient (panels a, c, e, g) and depolarization ratio (b, d, f, h) curtains for 23, 25, 29 June, and 1 July. Note the different latitude domains for each date are centered on CALIOP's intersection with the aerosol layer. The orbit segments are plotted in the applicable panels in Figure 3. Figure S2 in Supporting Information provides a closer view of the δ signal and statistics of these scenes.

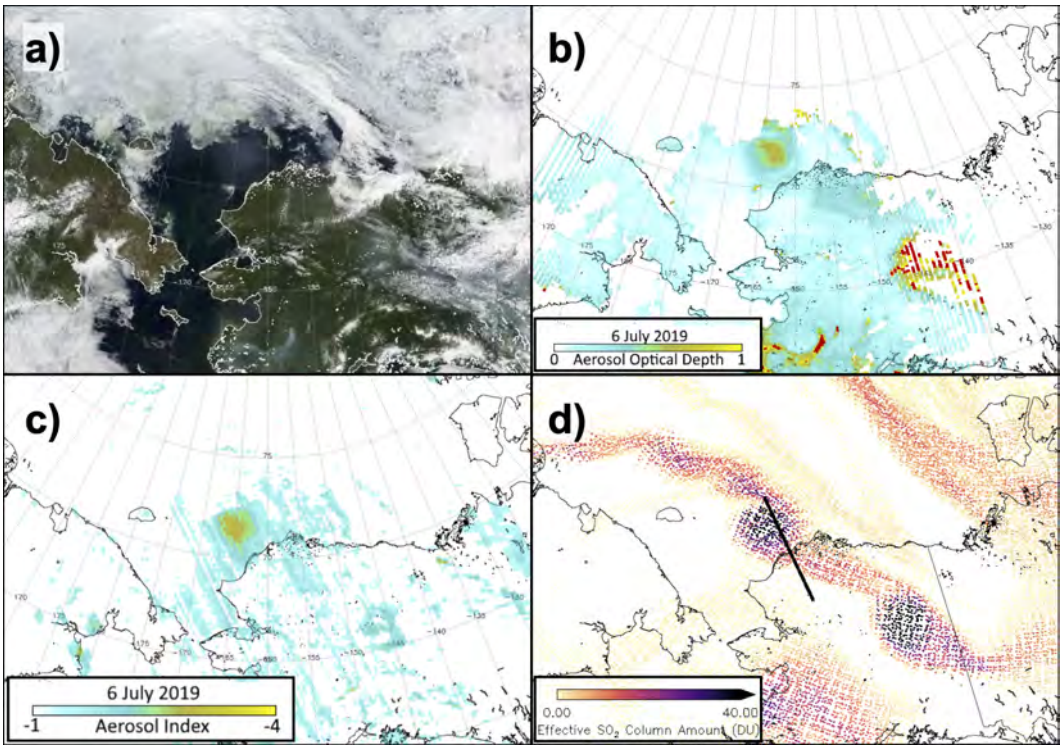

Figure 6. Multi-instrument display of the Raikoke aerosol and SO_2 SSACC on 6 July 2019. (a), Terra MODIS true-color visible, 23:00 UTC; (b), Terra MODIS corrected AOD (see text for details); (c), NOAA 20 OMPS scattering aerosol index, 22:31 UTC; (d), descending IASI SO_2 from the linear retrieval, 23:00 UTC. CALIPSO orbit segment, at 22:58 UTC, (See Figure 7) is overlain (d).

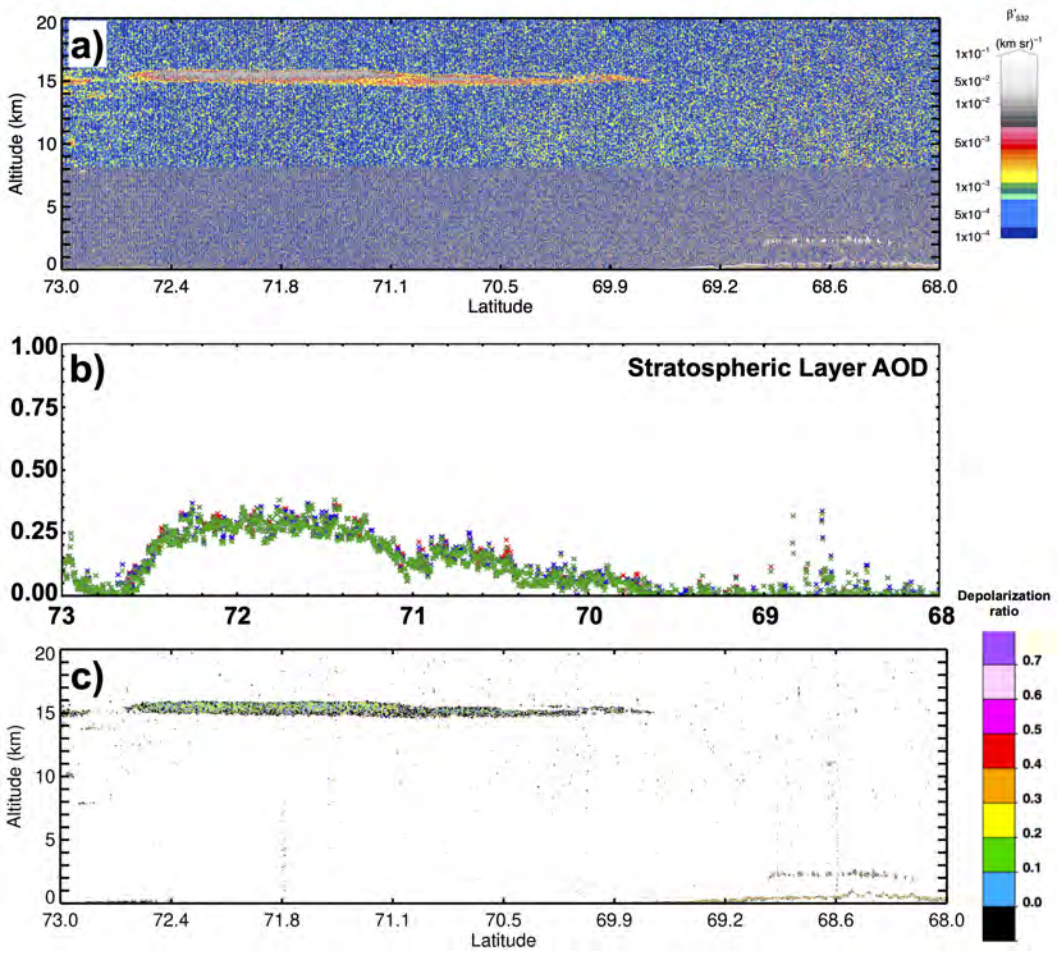

Figure 7. CALIOP daytime intercept of Raikoke 6 July SSACC. (a), β_{532}; (b), AOD, (c) δ. See text for details.

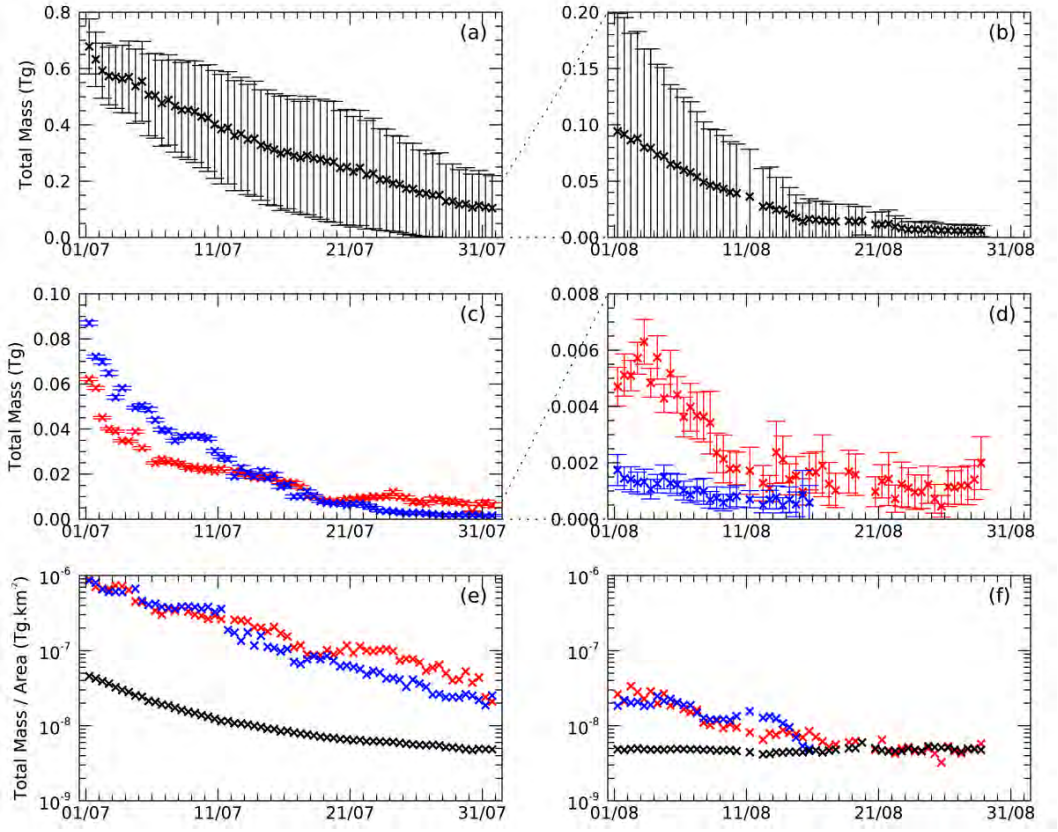

Figure 8. IASI SO_2 mass time series. (a) Total mass of SO_2 across the Raikoke cloud for 1-31 July 2019. (b) Same as (a) for 1-31 August 2019. (c) Total mass of SO_2 in the north (blue) and south (red) SSACCs for 1-31 July 2019. (d) Same as (c) for 1-31 August. (e) The mass of SO_2 per km^2 for 1-31 July. (f) Same as (e) for 1-31 August.

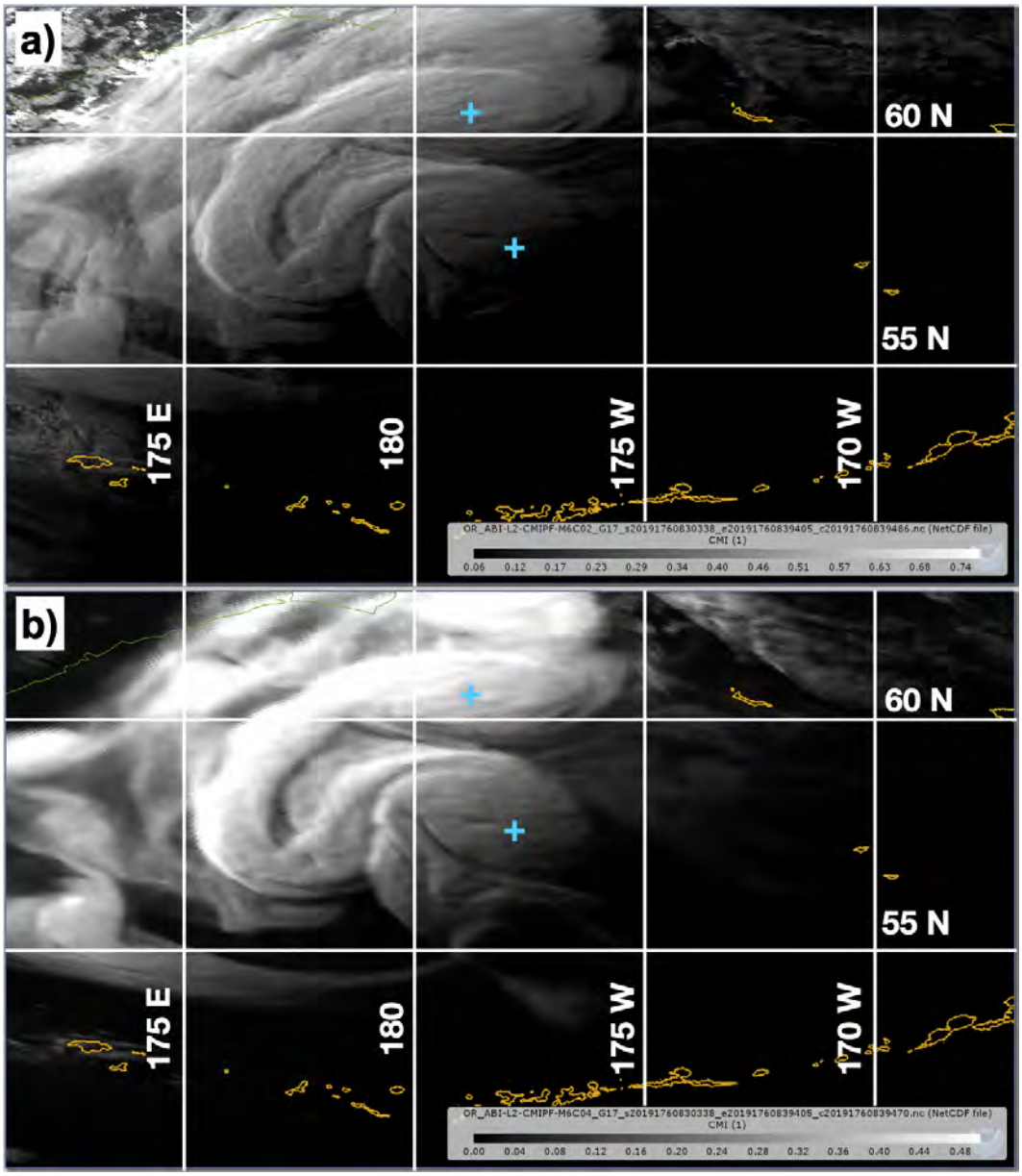

Figure 9. GOES 17 view focused on an oceanic scene north of the Aleutian Island chain on 25 June, 08:30 UTC. (a), 0.64 µm visible reflectance; (b), 1.37 µm cirrus channel reflectance. Blue "+" guide the eye to the SSACCs.

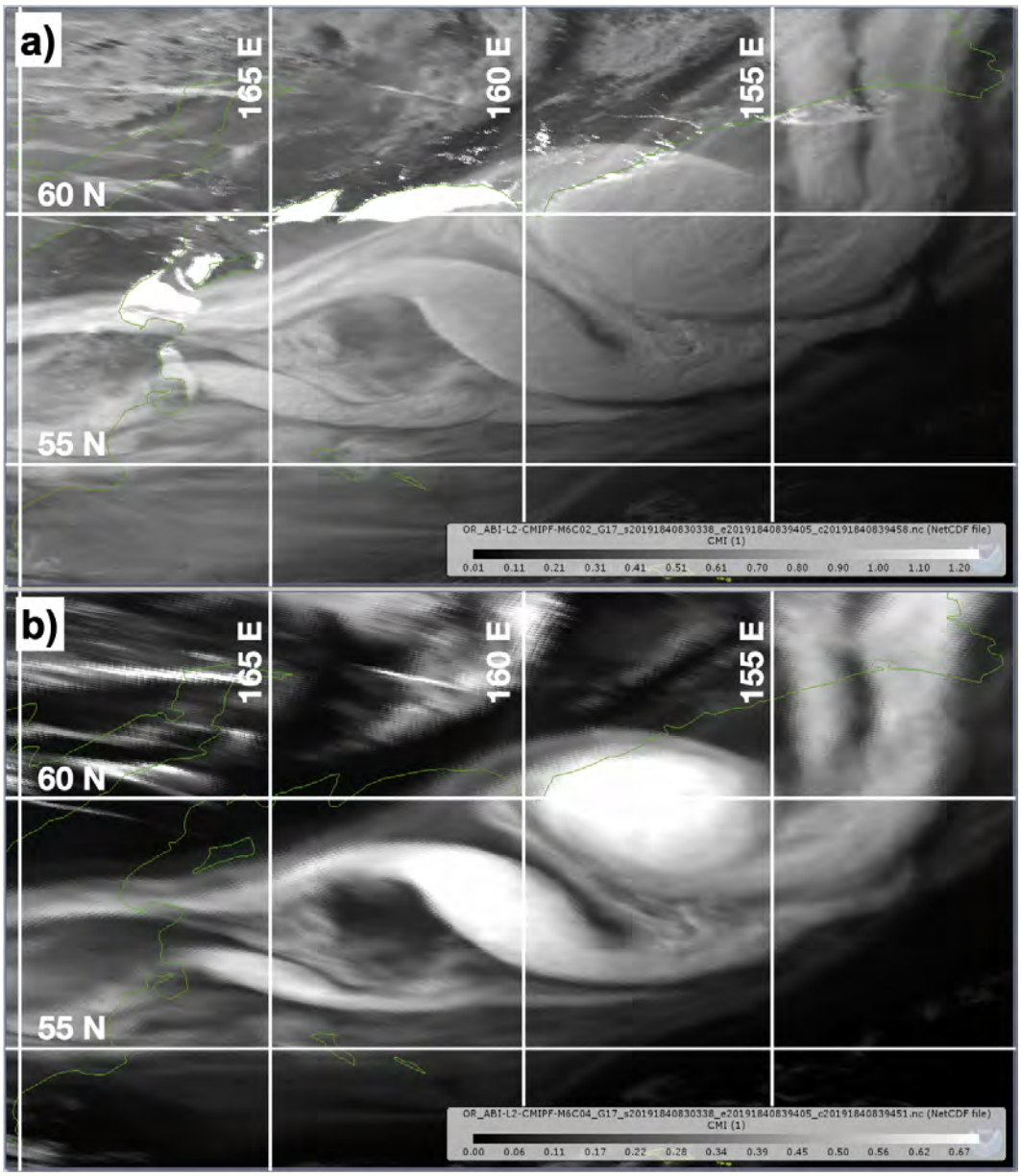

Figure 10. GOES 17 view focused on an oceanic scene off the eastern Siberian coast on 3 July, 08:30 UTC. (a), 0.64 μm visible reflectance; (b), 1.37 μm cirrus channel reflectance.

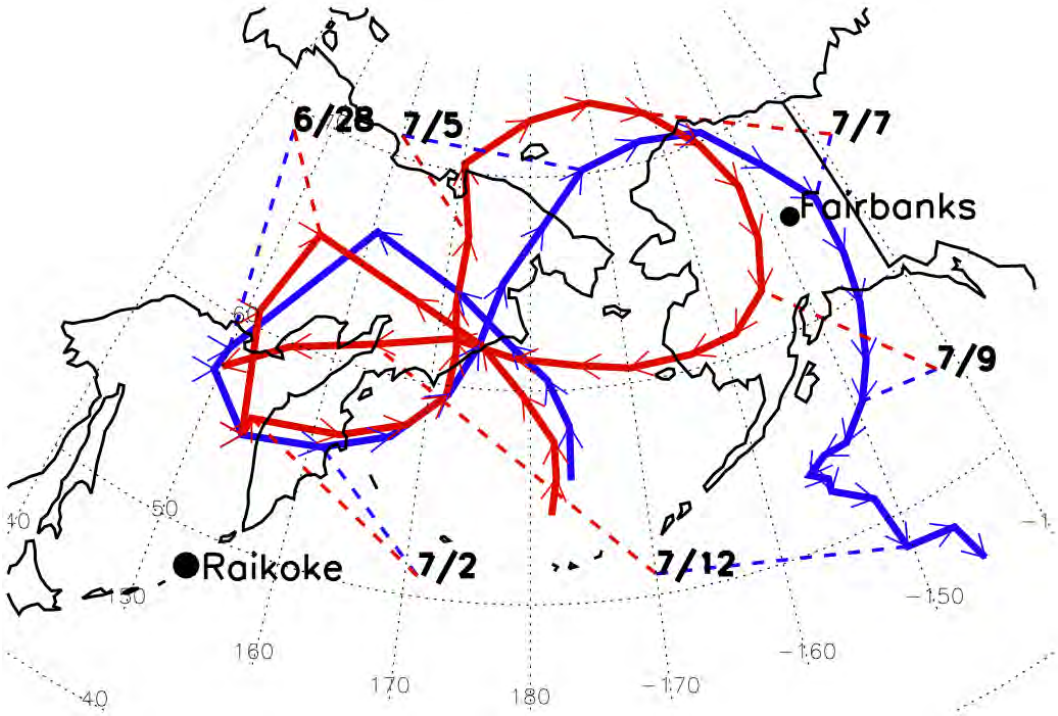

Figure 11. SSACC centroid locations mapped between 24 June and 13 July 2019. Based on twice-daily GOES West visible images. See text and Supporting Information for details. The red and blue paths follow the South and North SSACCs, respectively. Arrows at each observation time point in the direction of SSACC movement. Positions of each on six annotated dates are identified with matching color-coded dashed lines. Raikoke volcano and Fairbanks, Alaska are also marked with black dots.

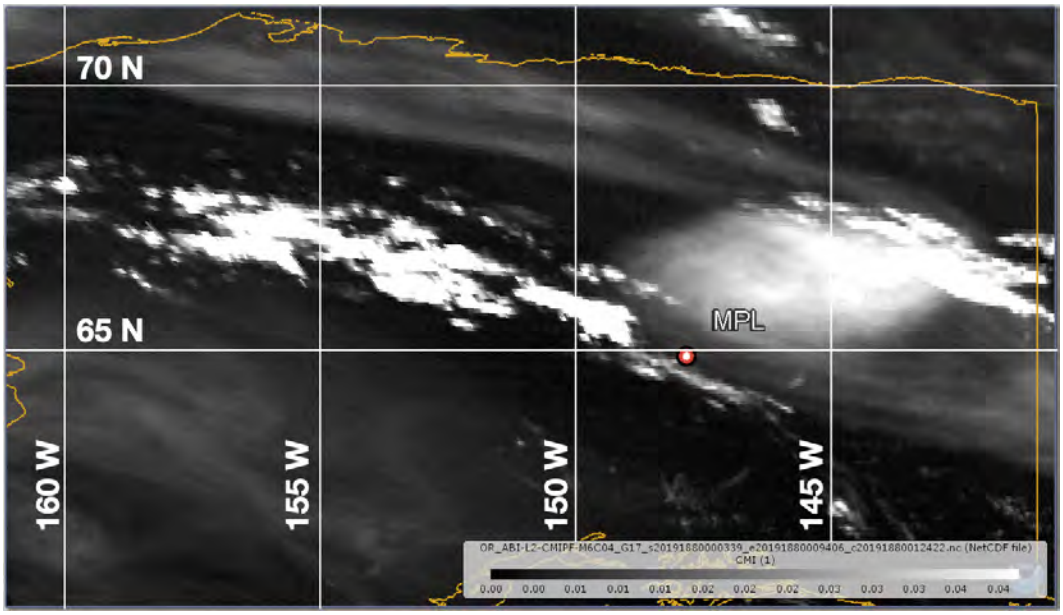

Figure 12. GOES 17 1.37 μm reflectance, 00:00 UTC 7 July. Fairbanks MPLNET and radiosonde-launch sites are both marked by the red dot labelled "MPL".

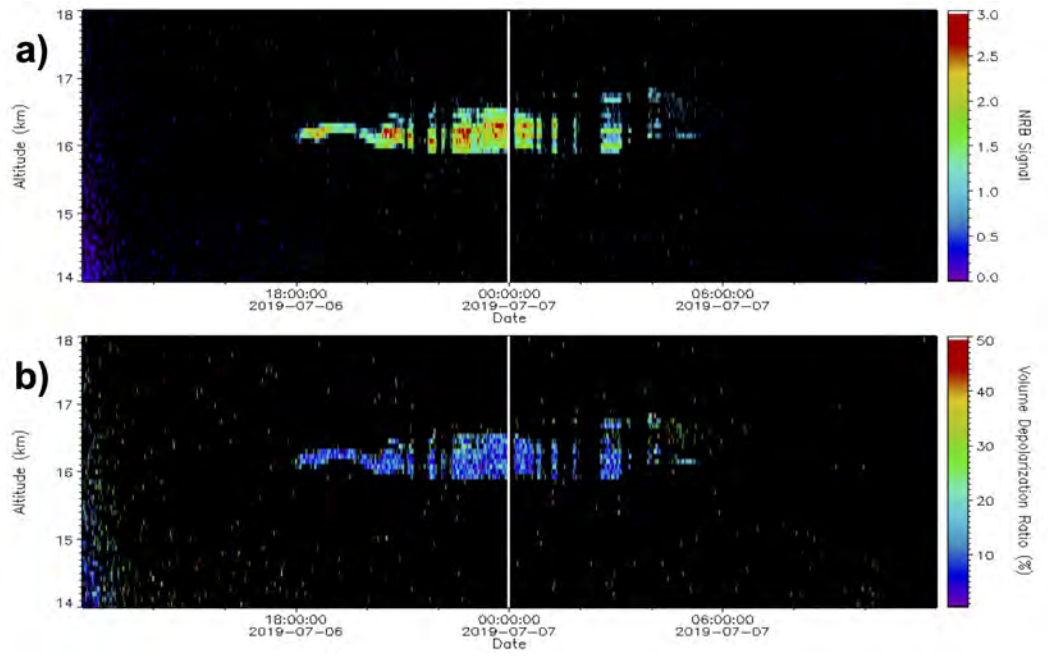

Figure 13. Fairbanks MPLNET height-time curtain from 12:00 UTC 6 to 7 July. (a), normalized relative backscatter. (b) volume depolarization ratio. Vertical white bar at 00:00 UTC marks the nominal radiosonde launch time.

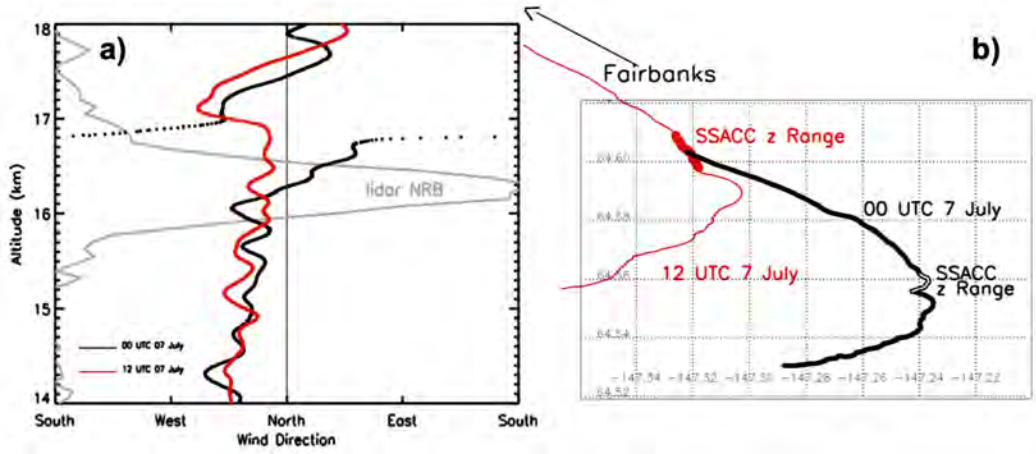

Figure 14. Fairbanks radiosonde wind direction and balloon position, 00:00 and 12:00 UTC 7 July. (a), wind direction, color coded per the legend. Overlain: MPLNET NRB profile (gray) at 23:58 UTC 6 July. Five-point (375 m) smoothing is applied. (b), mapped GPS balloon positions for altitudes between 13-22 km. Black for 00 UTC SSACC encounter), red, for 12 UTC (post-SSACC). SSACC-encounter altitude segment (15.9-16.8 km) at 00 UTC is annotated and highlighted by interior white. The 12 UTC balloon path highlights the altitude range of the SSACC with wider symbols and annotation. Arrow shows direction to Fairbanks origin.

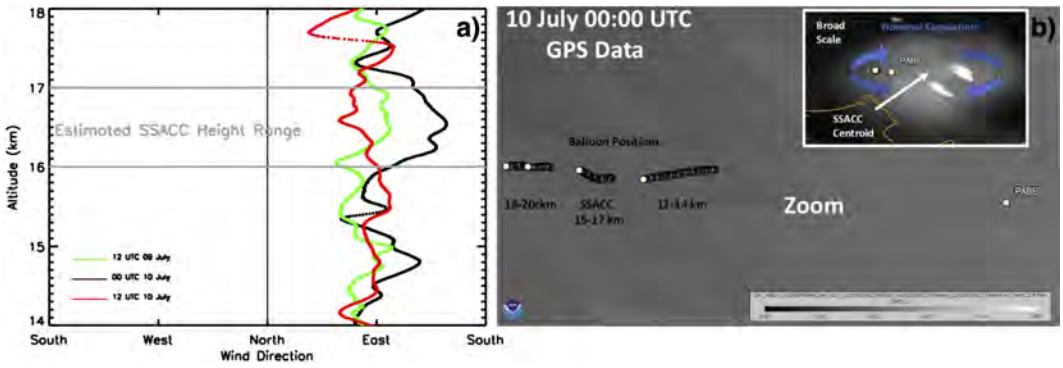

Figure 15. Bethel Alaska radiosonde (Upper air station ID: "PABE") wind direction and balloon position. (a), wind direction, color coded per the legend, for 12:00 UTC 9 July, 00:00 and 12:00 UTC 10 July. Overlain: approximate SSACC height range (gray lines). (b), mapped GPS balloon position. Inset shows wide scale view illustrating the GOES cirrus-channel reflectance at 00:00 10 July, approximate SSACC centroid, and blue arrows illustrating a notional anticyclonic closed circulation. Main map zooms in and shows details of the PABE location and balloon positions below, inside, and above the SSACC.

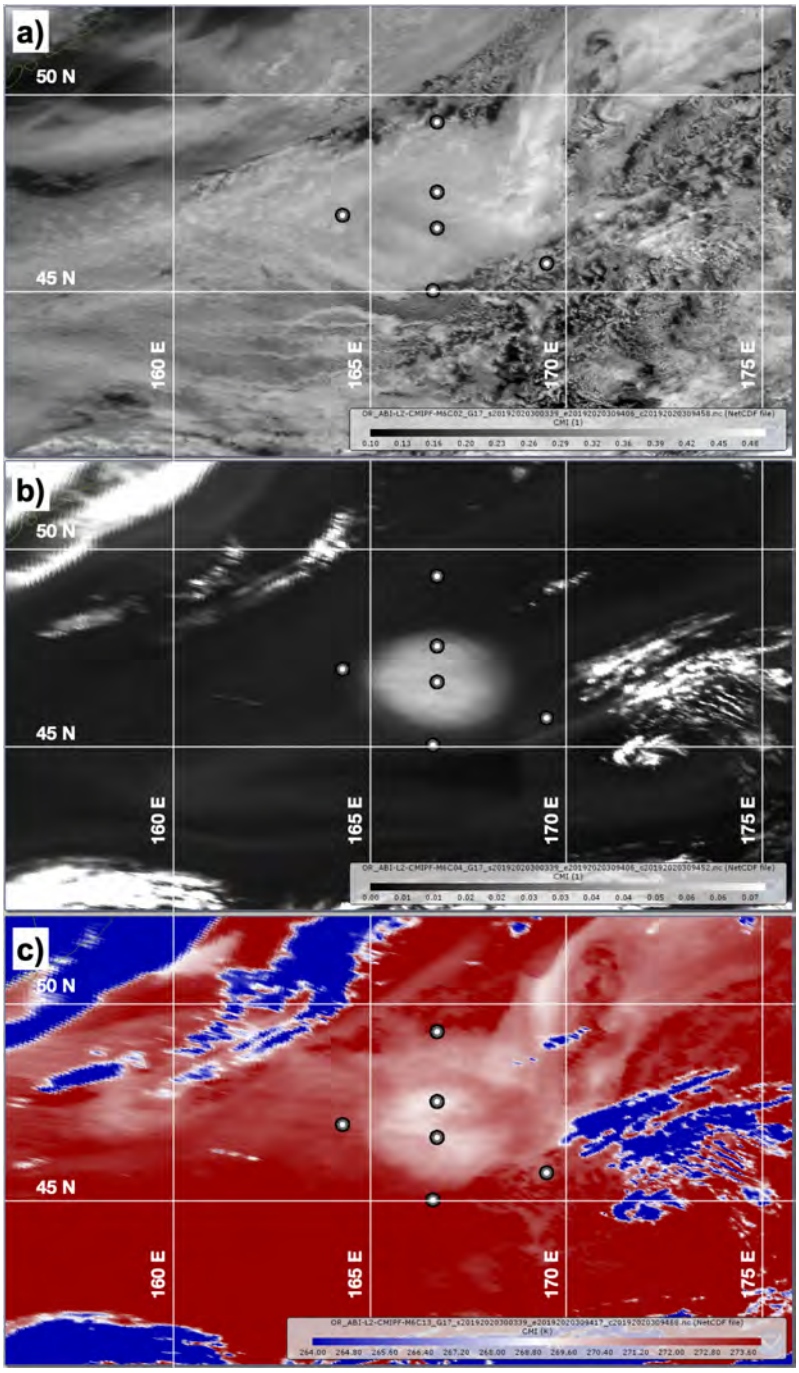

Figure 16. Multi-spectral GOES 17 imagery of South SSACC at 03:00 UTC 21 July. Dot markers indicate sampled pixels within and surrounding the SSACC; see text and Supporting Information for details. (a), 0.64 μm reflectance. (b), 1.37 μm reflectance. (c), 10.3 μm brightness temperature. The blue-white-red color bar and BT range guide the eye to BT values (see the legend) distinguishing South SSACC.

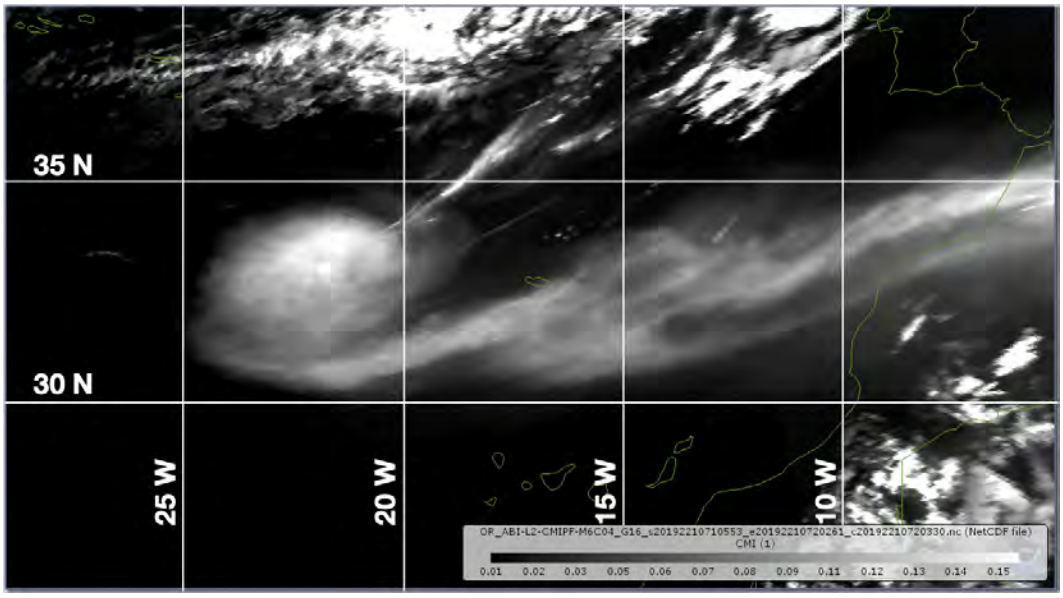

Figure 17. South SSACC over the Atlantic Ocean west of Africa on 9 August. GOES 16 1.37 μm reflectance at 07:10 UTC.

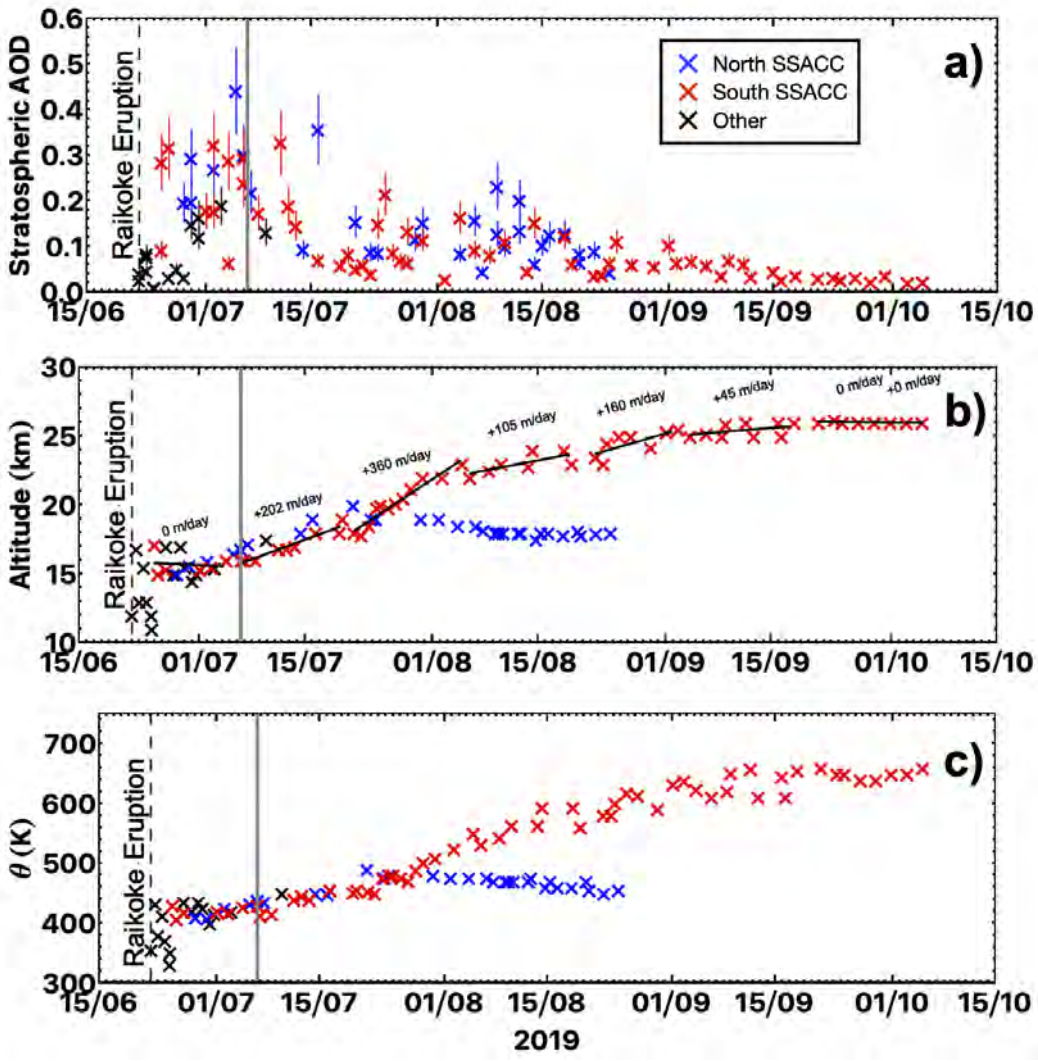

Figure 18. CALIOP SSACC-relative time series, 23 June-5 October 2019. (a), AOD_{mean}. (b), SSACC height in km. (c), SSACC potential temperature. Note the black "×" symbols are from the early days of cloud evolution when the SSACCs were difficult to discern independently or occupied the same scene. Vertical gray line corresponds to Fairbanks MPLNET measurement from Figure 13.